

From discrete to continuum modelling of boundary value problems in geomechanics: An integrated FEM-DEM approach

Jacques Desrues¹  | Albert Argilaga² | Denis Caillerie¹ | Gaël Combe¹ | Trung Kiên Nguyen³ | Vincent Richefeu¹ | Stefano Dal Pont¹ 

¹University of Grenoble Alpes, CNRS, Grenoble INP, Grenoble, France

²Urban and Environmental Engineering/Geomechanics, University of Liege, Liege, Belgium

³Ministry of Agriculture and Rural Development, Hanoi, Vietnam

Correspondence

Stefano Dal Pont, University of Grenoble Alpes, CNRS, Grenoble INP, 3SR, F-38000 Grenoble, France.
Email: stefano.dalpont@3sr-grenoble.fr

Funding information

TEC21, Grant/Award Number:
ANR-11-LABX- 0030; GRICAD Infrastructure, Equip@Meso Project, Grant/Award Number:
ANR-10-EQPX-29-01

Summary

Double-scale numerical methods constitute an effective tool for simultaneously representing the complex nature of geomaterials and treating real-scale engineering problems such as a tunnel excavation or a pressuremetre at a reasonable numerical cost. This paper presents an approach coupling discrete elements (DEM) at the microscale with finite elements (FEM) at the macroscale. In this approach, a DEM-based numerical constitutive law is embedded into a standard FEM formulation. In this regard, an exhaustive discussion is presented on how a 2D/3D granular assembly can be used to generate, step by step along the overall computation process, a consistent Numerically Homogenised Law. The paper also focuses on some recent developments including a comprehensive discussion of the efficiency of Newton-like operators, the introduction of a regularisation technique at the macroscale by means of a second gradient framework, and the development of parallelisation techniques to alleviate the computational cost of the proposed approach. Some real-scale problems taking into account the material spatial variability are illustrated, proving the numerical efficiency of the proposed approach and the benefit of a particle-based strategy.

KEYWORDS

DEM, double-scale approach, FEM, granular materials, numerical modelling, second gradient regularisation

1 | INTRODUCTION

The last decade has been a time of major changes in both experimental and modelling fields in solid mechanics, as a consequence of notable progress in instrumentation technology and computing power. On the experimental side, high-resolution imaging devices, fast data transmission, and large terabytes data storage have enabled an accelerated development and large diffusion of 2D then 3D imaging methods, using different kind of tomographic modalities (X-rays, neutrons, acoustic emissions, etc) and providing a wide range of resolution, both spatial and temporal. Large instruments facilities as, for example, synchrotron facilities (ESRF in Grenoble, France; Spring-8 in Hyogo, Japan; and APS in Chicago, USA) have opened access to scientific teams over the world to high-resolution and fast-imaging methods allowing to characterise the microstructure of materials and its variability inside structures, both natural and artificial. Both deformation

and microstructural changes occurring during loading processes applied to specimens and structures *in situ*, ie, inside the imaging installation, have become accessible to virtually any researcher, revealing the intimate features of deformation and degradation—or healing if any—processes in materials and structures. The increase in computing power of current workstations has enabled to develop CPU-demanding digital image correlation methods, which are able today to accurately and efficiently measure the strain fields in overall heterogeneous structures in 3D, along series of successive loading increments eventually leading to failure.

On the modelling side, the fast increase of computing power available and parallelisation methods that can handle a large number of cores in a single but distributed modelling process have made possible to address strongly CPU-demanding applications in engineering as well as fundamental studies.

The simultaneous progresses of the experimental and modelling tools available have fostered the development of the field of multiscale analysis. Today, to study the behaviour of a complex structure, it is not necessary anymore to ignore or oversimplify the real microstructure of its constitutive material: Both experimental and modelling tools have become available to undertake multiscale analysis of the structures.

This paper is devoted to the so-called concurrent double-scale numerical analysis of geomechanical problems involving granular media, purely frictional like dry sands, frictional cemented like sandstones, or friction cohesive like unsaturated sands.

1.1 | Discrete versus continuum modelling of granular media: cutting the gordian knot

It is commonly admitted that discrete modelling better represents the physics and the behaviour of granular media than the continuum mechanics framework, in which the specificities of the interaction between individual grains are not directly taken into account but incorporated into refined, carefully calibrated mathematical formulation of their overall behaviour as experimentally characterised over sets of well-chosen testing paths. The first approach is implemented in the so-called discrete element method (DEM), which has demonstrated its ability to represent all the very subtle aspects of the behaviour of the granular media: internal friction, dilatancy and contractancy, incremental non-linearity, memory effects under cyclic loading, inherent and acquired anisotropy, response to principal stress rotation and so forth. As a matter of fact, the constitutive behaviour rendered by the DEM model relies solely on the memory physically embedded in the material, that is, at a given time, the position of the grains, the list of contacts between grains, and the forces acting at these contacts. More complex models may take into account more advanced details of the grain assembly, eg, the grain shape, but already the simplest DEM model surpasses the most elaborated continuum-based constitutive equations by its ability to reproduce altogether, maybe in a crude way, the above evoked challenging characteristics of real granular media. On the other hand, the computational cost of DEM is by essence directly dependent upon the number of grains taken into account in the model. Even if the limit number of grains sustainable in a practical computation has increased by orders of magnitude since the first implementations of DEM in the late¹ the all-grain modelling of a geotechnical engineering problem with the real grain size distribution is still out of the scope: simply consider that a cubic metre of spheres of a diameter of 0.3 mm perfectly disposed in rows and columns—a much looser arrangement than in a real sand deposit—already contains 3.7×10^{10} grains! Considering coarser grains than the real ones is questionable in principle, especially if localised strains are expected to occur, since it is well known that the thickness of the shear bands in granular media is dependent upon the grain size.

Conversely, the continuum approach using the so-called finite element method (FEM) is well adapted to real-scale engineering problems. A reasonably fine discretisation will lead to a geometry containing a few thousands of elements, sometimes more, which can be dealt with an acceptable computational cost. Moreover, coupling with other physical processes like pore fluid flow, heat transfer, or chemical reactions is currently mastered in this computing framework. The drawback has already been mentioned: The constitutive equations used to represent the mechanical behaviour of the granular materials hardly take simultaneously into account all the different aspects of its response: a choice between cyclic response, anisotropy, and principal stress rotations is required when selecting a constitutive model, and some features have to be neglected.

So the “Gordian Knot” challenge here consists in the choice of the best modelling strategy for an engineering problem, between DEM and FEM, knowing that both present severe impediments.

The double-scale numerical approach proposes to simply cut the knot, ie, refuse to choose; instead, use simultaneously both methods for what they are good at, in an integrated numerical process that consists in replacing the constitutive equation by a DEM process at the small scale, inside a FEM process developed at the large scale.

1.2 | Double-scale numerical approach as a homogenisation method

The idea of modelling the mechanical response of a microstructure—possibly coupled with other physical processes like in thermo-mechanical or hydro-mechanical processes—with a view to up scaling the results of that microscale analysis to the macroscopic scale of a structure, is far from being new. Homogenisation methods have been developed in this spirit for decades, leading to remarkably refined theoretical works, which, in general, result in precious information on the form that a macroscopic constitutive equation should have to accurately represent the considered medium. In the classical approach, the microscale analysis, whatever theoretical or numerical, is performed separately and independently of a possible macroscale analysis using the homogenised model. It is not in the scope of the present paper to enter in a review of the large field of homogenisation methods. Instead, the paper will focus on a double-scale numerical homogenisation method, involving FEM at one scale and DEM at the other scale. That is the reason why it is entitled here as FEM×DEM, the cross “ \times ” aiming at underlining the strong intrication of the two methods in the numerical process.

1.3 | Concurrent double-scale numerical modelling

The method discussed in this paper can be described as a double process, which involves simultaneously solving a boundary problem at the microscale, playing the role of a numerical homogenisation method, and solving the macroscale boundary value problem representing the geostructure to be analysed, both processes exchanging information all along the course of the problem solving.

The key point in this method lies in the fact that the microscale computation, a DEM computation in this instance but can be a FEM computation as well, plays the role of the constitutive law for the macroscopic computation. Given a macroscopic strain, it returns the corresponding macroscopic stress. It is used exactly as any other macroscopic constitutive law. Although an increasing number of teams in the world are developing this kind of numerical approaches, the vocabulary to designate this framework is not yet completely fixed: The words “hierarchical,”² “integrated,”³ or “concurrent”³ can be found in the literature. All of these wordings point out the imbrication of the two processes. Here, we will use the latter definition.

Generally speaking, scale-bridging methods aim at establishing a coupling between the macroscale observable behaviour(s) such as plasticity, elasticity, damage, thermo-mechanical and hydro-mechanical coupling and so forth and microscale phenomena as various as contrasting mechanical (or other physical) properties in composite materials, dislocations in polycrystalline materials, microcrack development in heterogeneous rocks, grain sliding and rolling in granular media, and others, eg, wall cells buckling in foams or phase changing particles embedded in composites. There is a large spectrum of scale-bridging methods from theoretical homogenisation allowing to formulate microscale-derived macroscale constitutive equations, to direct micro-macro methods like the one presented in this paper. A comprehensive review of the different approaches entering in this large spectrum has been proposed in Kanouté et al.³ In the case of direct micro-macro methods, concurrently with the macroscale analysis of the structure performed using FEM, an analysis of the microscale elementary volumes attached to every integration points in the discretised structure is performed: A presentation of trends and challenges of this approach is presented by Geers et al.⁴

Among concurrent multiscale methods, most have been developed using FEM at both the macroscale and the microscale: They are called FE² methods, introduced among others by Feyel cited by Kanouté et al.³ In the context of geomaterials, FE² can be used for problems involving potentially microcracked rocks, with hydromechanical coupling directly taken into account at the microscale as discussed in Chambon, Bésuelle, van den Eijden et al.^{5,6} However, as far as granular materials are concerned, using the so-called DEM to analyse the microscale REVs is most attractive, since this method captures directly the granular nature of the material with its specific features: internal friction and dilatancy/contractancy.

1.4 | DEM-based upscaled constitutive equations

Before going to the true double-scale numerical concurrent analysis, it is worth citing here some works that have been devoted specifically to the study of the constitutive equation (CE) derived numerically using DEM as a microscale computational tool. In some way, most works developed in the DEM and molecular dynamics community could be considered as entering this category—with the exception of works devoted to direct DEM modelling of engineering applications. Hence, not pretending to be exhaustive, we restrict here to a few examples of works that were clearly dealing with the homogenised constitutive law that can be derived numerically from the DEM model. The response of such directly DEM-derived CE can be analysed using so-called “response envelopes” as defined by Gudehus.⁷ A comparison of response

envelopes resulting from DEM and extended plasticity theories such as bounding surface plasticity, generalised plasticity, and generalised tangential plasticity has been presented by Tamagnini et al.⁸ showing that DEM-derived CE allows for complex incrementally non-linear features such as plastic strains occurring for (almost) all probing directions starting from a preloaded state, better than generalised plasticity models can do. Other studies have been devoted to the derivation by DEM simulations of the tangent operator for a given loading path applied to an elementary volume (EV) of granular material. Borja et al^{9,10} studied the overall constitutive relation resulting from DEM and presented a methodology for calculating the overall tangential moduli for periodic assemblies of circular disks, obtained from a linearisation of the overall constitutive relation. Meier et al¹¹ present a FEM×DEM double-scale modelling approach of a geostructure, namely, a classical slope stability problem, and propose to use a consistent tangent operator derived using the assumption that all particles in the granular volume are mapped by the macroscopic deformation tangent tensor, hence excluding any fluctuation at the microscale level. At the price of disregarding the effects of the morphology of the granular assembly, quadratic convergence is obtained in the Newton-Raphson iterations of the FEM problem. In other studies, the tangent operator, or overall tangential moduli, can be used to analyse the onset of localised deformation, along the lines of Rudnicki and Rice.¹² This specific subject has been addressed, eg, by Wren et al¹⁰ and Nitka et al.¹³

Andrade et al¹⁴ have presented a multiscale original approach for granular media that is close to the direct micro-macro approach discussed in the present paper, which still makes use of an elastoplastic constitutive model at the macroscale instead of using a DEM simulation as a constitutive relation. In their study, experimental results using digital image correlation (DIC) on 3D numerical images of specimens subjected to triaxial tests with X-ray tomography are used to extract some plastic internal variables that are involved subsequently in the macroscale constitutive model.

1.5 | FEM×DEM true concurrent multiscale models

Restricting now the scope of the paper to implementations of true double-scale concurrent analysis in a operational computational framework, a number of studies can be identified in the last decade. First, feasibility demonstrations involving simple macrostructures with more or less coarse meshes have been published by Kaneko,¹⁵ Meier et al.,¹⁶ Miehe et al.,^{17,18} Nitka,¹⁹ and Guo and Zhao.^{2,20} Kaneko et al¹⁵ are probably the first to assemble a FEM and a DEM code in a concurrent double-scale computing architecture and to illustrate the capacity of the method to model a macroscale biaxial test up to well-developed shear band formation. Nitka et al¹⁹ present the multiscale modelling of oedometric and biaxial drained and undrained tests on 2D granular media; Zhao and Guo² model a drained biaxial test at different initial void ratio, showing a coarse but distinguishable strain localisation of both deviatoric strain and fabric. Miehe et al¹⁸ model a biaxial test, showing strain localisation starting from the lateral boundary close to the corners of the specimen.

Later on, these pioneering works have been extended to more realistic macrostructures, allowing to illustrate different achievements and advantages of the double-scale approach. Guo and Zhao with different co-authors have addressed different subjects such as anisotropy, fabric evolution and strain localisation,²¹ hydro-mechanical coupling,²² application to geotechnical engineering problems,²³ and compaction bands.²⁴ Desrues and co-authors have showed applications of the method to strain localisation studies in biaxial test and field problems, namely, gallery excavation (convergence-confinement method) and cylindrical cavity expansion (in situ pressuremetre test).²⁵⁻²⁹ To eliminate the well-known mesh-dependency effect on strain localisation prediction in FEM models, they have used second gradient regularisation, which proved to be fully compatible with double-scale approach.²⁸⁻³⁰ Argilaga et al^{28,31} point out the role of the Newton-Raphson operator in the convergence of the FEM×DEM models; Ghassan et al³² study the effect of variability of the DEM elementary volume in the response of the double-scale method applied to a biaxial test. Several works implement 3D DEM instead of simple 2D disks at the microscale: Guo et al²¹ and Nguyen et al.³⁰

In this paper, we present first the DEM aspects of the building of the DEM-based CE and then the FEM aspects, namely, the particularities of using such a CE in the Newton-Raphson iterative process. A section is devoted to the parallelisation strategies to be used to overcome the CPU cost issue. The introduction of an internal length to regularise the macroscale boundary value problem (BVP) is discussed in another section, and then some examples of BVP solving are presented. The last section present a study of the effects of spatial variability at the macroscale induced by selecting a set of slightly different elementary volumes, and then conclusions and perspectives are drawn.

In this paper, the following conventions are adopted for the notations: (1) “usual” vectors like positions or forces are denoted with overarrowed variables (eg, \vec{x} and \vec{f}); (2) second-order tensors like Cauchy stress or deformation gradient are denoted with bold characters (eg, σ and F); (3) the dot symbol denotes for the simple contraction between two tensors (eg,

$\vec{T} = \sigma \cdot \vec{n}$; (4) the colon symbol denotes for the double contraction of two second-order tensors (eg, $\sigma : \epsilon$); (5) the tensorial product $\vec{a} \otimes \vec{b}$ states for the linear application defined by $\forall \vec{c}, (\vec{a} \otimes \vec{b}) \cdot \vec{c} = (\vec{b} \cdot \vec{c}) \vec{a}$; (6) the wedge symbol \wedge denotes for the cross product; and (7) whenever the index notation of tensors is used, the Einstein notation for the contraction of tensors is used.

2 | CONCURRENT DOUBLE-SCALE COMPUTING SCHEME

2.1 | Double-scale coupling

The concurrent double-scale computing scheme illustrated in Figure 1 essentially rely on three key points:

1. a constitutive equation at the macroscale can be derived from the resolution of a DEM-based boundary value problem on an elementary volume defined at the microscopic scale; this constitutive equation can be called “Numerically homogenised Law” (NHL); it is represented in Figure 1 by the box framed with dotted lines;
2. this can be done for a set of elementary volumes distinctly attached to every integration point of the macroscale FEM model; in Figure 1, one specific element of the macroscale structure is extracted as an example, highlighted in green, showing its four integration points commonly referred to as “Gauss Points”;
3. this can be done concurrently by a number of numerical processes running the computations independently at the macroscale (one process) and the microscale (several processes).

As illustrated in the figure, the NHL plays exactly the role of a constitutive equation in the FEM framework, as it takes as an input of the deformation gradient specific to the integration point, and returns the actualised stress tensor and a “tangent” operator. More will be explained later about the different options as far as the operator is concerned.

Clearly, a *sequential* implementation of this computing scheme would be extremely time consuming, since the sequential flow chart would consist in solving one after the other all the microscale DEM problems and assembling their contributions to the FEM linear system, then solving the latter and iterating these steps until the macroscale equilibrium is met, for a given macroscopic loading step. Hopefully, the microscale problems can be run separately using parallelisation procedure; such parallelised process can be extremely efficient since the microscale computation is likely to be the most CPU-demanding part of the process, depending on the relative complexity of the macro and micro models, respectively.

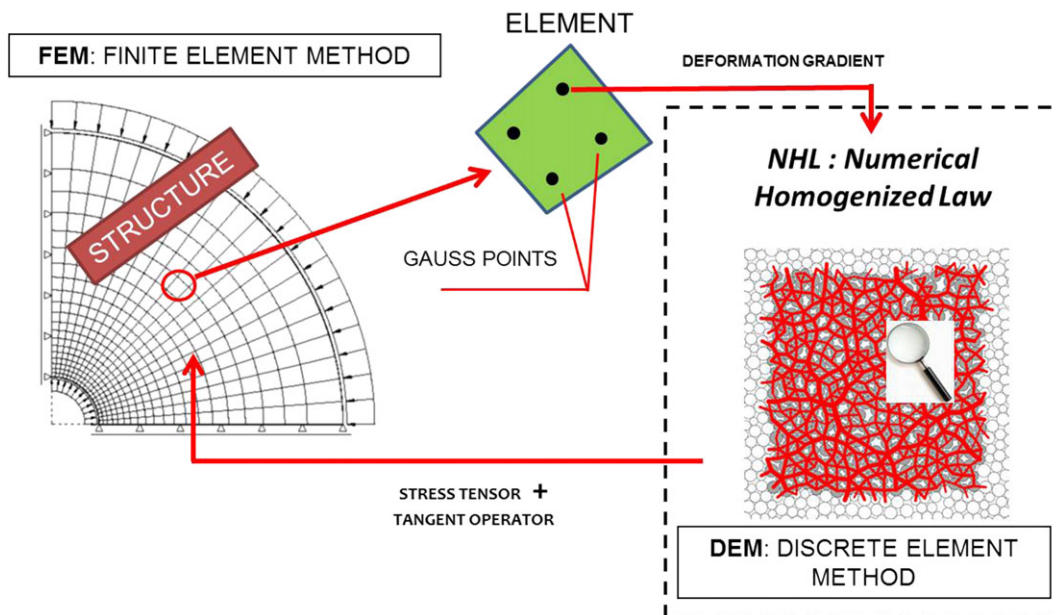


FIGURE 1 FEMxDEM principle: discrete element method (DEM) is used to define a Numerically Homogenised Law (NHL) from the boundary problem modelling the specific deformation process applied to the elementary volume attached to every gauss point in the macrostructure [Colour figure can be viewed at wileyonlinelibrary.com]

2.2 | NHL-DEM: A DEM-based constitutive law

Granular materials, considered as continuous media, are anelastic, which implies that their constitutive equations are path dependent. Consequently the determination of the deformation of such materials is necessarily an evolution problem, generally considered to be quasi-static, thus requiring the implementation of a time stepping method. In what follows, the left-limit and the right-limit states of a loading increment are respectively specified by the superscripts i and f . In all equations and illustrations that follow, the 2D or 3D particles are assumed to be circular or spherical, respectively. Usually the constitutive equation of the granular materials, which can be, for instance, elasto-plastic or hypo-plastic or a damage one model, is used to yield a relation giving the Cauchy stress σ^f at the end of a time step in terms of the deformation gradient F^f at the end of a time step, which can be written as follows:

$$F^f \mapsto \sigma^f = S(F^f), \quad (1)$$

which is a relationship that, strictly speaking, is not a constitutive equation but rather an *integrated* constitutive equation. The function S , which can involve different parameters as the values σ^i and F^i at the beginning of the step of σ and F , has to be determined for each time step. The boundary value problem to be solved at the end of each step consists of the balance equation of the unknown configuration Ω^f at the end of the time step, the “integrated constitutive equation” (Equation 1) and c equation reads as follows:

$$\forall \vec{w}^*, - \int_{\Omega^f} \sigma^f : \epsilon(\vec{w}^*) \, dv + \int_{\partial\Omega^f} \vec{F}^f \cdot \vec{w}^* \, ds + \int_{\Omega^f} \vec{f}^f \cdot \vec{w}^* \, dv = 0, \quad (2)$$

where $\epsilon(\vec{w}^*) = (\nabla \vec{w}^* + \nabla \vec{w}^{*T})/2$ is the virtual strain rate, \vec{F}^f is the boundary force density term, and \vec{f}^f represents the body force density. It is nonlinear and needs to be solved using some suitable method, usually the Newton-Raphson's method, which in turn needs to differentiate the function S . Depending on the considered constitutive equation, the differentiation that leads to the so-called consistent operator can be problematic; that point is developed and discussed in Section 2.5 in which some alternative operators are presented and tested.

In a FEM×DEM procedure, the “constitutive equation” (Equation 1) is directly provided by the DEM computing of the dynamic motion of the grains of a given assembly. There are different ways to submit an assembly of grains to a deformation gradient F^f in order to induce a motion of the grains: In this work, the so-called periodic conditions are used. This means that, at any time, the assembly of grains is considered to be the elementary cell of a periodic granular medium of vectors of periodicity \vec{Y}^α , $\alpha = 1, 2, 3$; see Figure 2. A central point in a DEM computation is the detection of contacts between grains, since grains interact only when they make contact. It is also worth noting that the periodic conditions create a particular situation; indeed, a grain of the elementary cell may make contact with grains of the elementary cell itself or with grains of a neighbouring one. In that case, see Figure 2; the grain n' of the elementary cell is reputed to make contact with the grain m' of the elementary cell, which corresponds by periodicity to the grain m' of the neighbouring cell. However, the geometry and the kinematics are those of the grain of the neighbouring cell. The implementation of the periodic conditions in the numerical code is detailed in Section 2.4. On a time step of the FEM computation, a deformation gradient F^f being given, the vectors of periodicity read as follows:

$$\vec{Y}^\alpha(t) = F(t) \cdot \vec{Y}_R^\alpha, \alpha = 1, 2, 3,$$

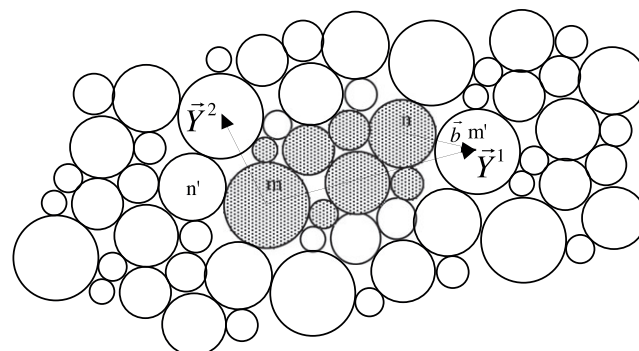


FIGURE 2 Example of a periodic granular medium—contact between a grain of the elementary cell and a grain of an adjacent cell

where the \vec{Y}_R^α s are the vectors of periodicity of the reference configuration of the elementary cell and $\mathbf{F}(t) \cdot \vec{Y}_R^\alpha$ denotes the image of the \vec{Y}_R^α by the linear application $\mathbf{F}(t)$. $\mathbf{F}(t)$ is given in term of \mathbf{F}^f by

$$\mathbf{F}(t) = \begin{cases} \mathbf{F}^i + (\mathbf{F}^f - \mathbf{F}^i) \frac{t}{\tau} & 0 \leq t \leq \tau \\ \mathbf{F}^f & \tau \leq t \end{cases}, \quad (3)$$

where the choice of the time τ takes care of the loading speed and relies on the inertial number; this point is discussed and detailed in Section 2.4; see Equation 18 (in those expressions, t is the time of the DEM computation).

The DEM computation consists in a time stepping integration of the dynamical equations of the motion of the grains. The computation is carried out until the total kinetic energy of the grains is almost 0, and very few contacts between grains are created or lost. The forces and moments applied to a grain are the contact forces and moments because of the other grains with which the grain makes contact. Those contact forces and moments depend on the positions, the rotations, and the corresponding velocities of the two grains making contact. The expressions of those constitutive equations for the contacts are partly incremental; in three dimensions, the requirement of the frame invariance of those constitutive equations arises; hence, it has to be resolved. Details are provided in Section 2.3.2.

At the end of the computation, the DEM provides the positions of the grains of the elementary cell as well as the contact forces. The Cauchy stress tensor is then assessed using the classical Cauchy-Poisson formula (see Section 2.4.2). In the end, the DEM computation yields σ^f in terms of \mathbf{F}^f , which defines the function S of Equation 1.

2.3 | Individual frame-invariant contact mechanical law

In many papers about DEM, the contact forces are presented more in the form of an algorithm than as a constitutive equation. For instance, in the pioneering work of Cundall and Strack,^{1, p 52, equations 14-19} the increment, over a DEM time step, of the contact force between grains is first evaluated as an elastic law, and then the force at the end of the step is checked against the Coulomb criterion, and finally, if needed, the tangential component of the force is reduced so as to satisfy the Coulomb criterion. The constitutive equation for the contact force presented in this paper, which is new, at least to the authors knowledge, is rather similar to the elasto-plastic one considered by Miehe and Dettmar.¹⁷ The main difference is that for the constitutive equation of Miehe and Dettmar, which is used in a 2D context, the question of frame invariance is almost pointless, whereas it is a strong requirement for a constitutive equation that is intended to be used in 3D DEM simulations. For that reason, the tangential part of the constitutive equation in Equation 5 is written in an incremental form. The frame invariance principle requires that any constitutive equation should keep the same form in any reference frame. A brief summary of reference frames and changes of reference frames is given in Appendix A.

2.3.1 | Contact forces

In order to give the expression of the contact force between two grains, this contact is orientated—that means that one grain is (arbitrarily) named the origin and the other the extremity of the contact (they can be also called master and slave or with any other bipolar names). In the following, the origin and extremity are denoted by n and m , and the radii of the grains are then R^n and R^m . The positions of the centres of the grains are \vec{r}^n and \vec{r}^m , the so-called branch vector is $\vec{b} = \vec{r}^m - \vec{r}^n$, and the normal at the contact is $\vec{n} = \vec{b}/\|\vec{b}\|$. The orthogonal space to \vec{n} is denoted by Π and $\mathbf{P}_\Pi = \mathbb{I} - \vec{n} \otimes \vec{n}$, where \mathbb{I} is the identity operator and denotes the orthogonal projection onto Π . \vec{v}^n , \vec{v}^m , $\vec{\omega}^n$, and $\vec{\omega}^m$ denote the translation and rotation velocities of the grains.

The action of the grain m on the grain n is assumed to be equivalent to a force \vec{f} applied at some contact point \vec{P} (see Figure 3), meaning that at that point, the moment applied by m on n is equal to 0. \vec{f} is decomposed into a normal component and a tangential one $\vec{f} = f_N \vec{n} + \vec{f}_T$. In the absence of cohesion, the normal component of the contact force is elastic and satisfies the so-called Signorini condition of unilaterality; this means that as a function of the overlap $d = \|\vec{b}\| - (R^n + R^m)$ of the two grains, it reads

$$f_N = \frac{k_N}{2}(d - |d|). \quad (4)$$

The law governing the tangential force is essentially incremental; it yields the time derivative $\dot{\vec{f}}_T$ in terms of the geometry and the kinematics of the two grains making contact and of the value of the tangential force. The motion of the grains may cause a change in the orientation of the normal \vec{n} , which induces a variation of the tangential force \vec{f}_T since \vec{f}_T lies in Π , the orthogonal space to \vec{n} . The derivation of the relation $\vec{f}_T \cdot \vec{n} = 0$ yields $\dot{\vec{f}}_T \cdot \vec{n} + \vec{f}_T \cdot \dot{\vec{n}} = 0$, which means that the

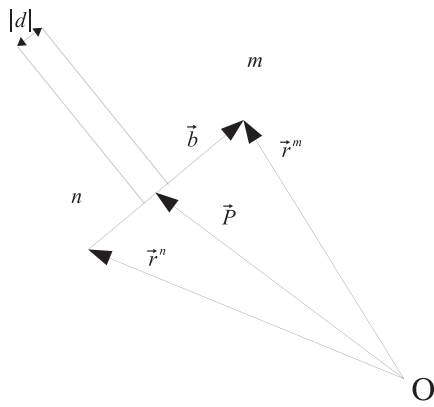


FIGURE 3 Two grains making contact—contact point \vec{P} , overlap d , and branch vector \vec{b}

normal component of $\dot{\vec{f}}_T$ is completely determined by the datum of \vec{f}_T and \vec{n} and consequently that the incremental law of $\dot{\vec{f}}_T$ may only concern the tangential component of $\dot{\vec{f}}_T$, it reads

$$\text{If } f_N = 0 \text{ then } \vec{f}_T = 0, \dot{\vec{f}}_T = 0 \quad (5a)$$

$$\text{If } f_N < 0 \text{ then } \|\vec{f}_T\| + \mu f_N \leq 0 \text{ and} \quad (5b)$$

$$\mathbf{P}_\Pi \cdot \dot{\vec{f}}_T = \mathbf{P}_\Pi \cdot \left(\frac{1}{2} (\vec{\omega}^n + \vec{\omega}^m) \wedge \vec{f}_T \right) + k_T (\vec{V}_T^r - \lambda \vec{f}_T), 0 \leq \lambda \quad (5c)$$

$$\lambda (\|\vec{f}_T\| + \mu f_N) = 0, \quad (5d)$$

where \wedge denotes for the cross-product and \vec{V}_T^r is the tangential component of the relative velocity of the grains at the contact point \vec{P} that reads as follows:

$$\vec{V}^r = \vec{v}^m - \vec{v}^n + \vec{\omega}^m \wedge (\vec{P} - \vec{r}^m) - \vec{\omega}^n \wedge (\vec{P} - \vec{r}^n). \quad (6)$$

The first term of the left-hand side of Equation 5c is perpendicular to \vec{f}_T ; consequently, only the fourth term $k_T (\vec{V}_T^r - \lambda \vec{f}_T)$ takes part in the evolution of the norm $\|\vec{f}_T\|$ of \vec{f}_T . Together with the inequalities of Equation 5b and of Equation 5a and with the consistent condition Equation 5d, that second term presents the characteristics of an elasto-plastic constitutive equation, but for the fact that it is purely incremental, it is close to the constitutive equation of contacts considered by Miehe and Dettmar.¹⁷ The term $\frac{1}{2} \mathbf{P}_\Pi \cdot (\vec{\omega}^n + \vec{\omega}^m) \wedge \vec{f}_T$ makes \vec{f}_T rotate around the normal \vec{n} ; it fulfills a part of the frame invariance of the law (see Section 2.3.2).

Equation 5c can be rewritten in a form that is more operable for the integration on a time step of the following section, it reads as follows:

$$\mathbf{P}_\Pi \cdot \dot{\vec{f}}_T = C_N \vec{n} \wedge \vec{f}_T + k_T (\vec{V}_T^r - \lambda \vec{f}_T), 0 \leq \lambda, \quad (7)$$

where $\vec{C} = \frac{1}{2} (\vec{\omega}^n + \vec{\omega}^m)$ and $C_N = \vec{C} \cdot \vec{n}$. Indeed for any vector $\vec{A} = A_N \vec{n} + \vec{A}_T$ with $\vec{A}_T \cdot \vec{n} = 0$ and any vector \vec{a} of Π , $\mathbf{P}_\Pi \cdot (\vec{A} \wedge \vec{a}) = A_N \vec{n} \wedge \vec{a}$ holds.

2.3.2 | Frame invariance

The principle of frame indifference, also called frame invariance or material invariance, stipulates that any constitutive equation of the mechanics should be frame invariant that is to say should have the same form in any frame. This principle has consequences about the form of the constitutive equations. The frame invariance of the constitutive laws of contact forces between grains is seldom considered in the literature, see Kuhn et al³³; it is true that many DEM calculations are performed in two dimensions, and in that case, the frame invariance of the contact laws is almost obvious.

The implementation of the frame invariance principle needs some mathematics, summarised in Appendix A.

The principle of frame invariance applies to the constitutive equation of the contact force between grains as a whole. It is clear from their definitions that the overlap d , the normal \vec{n} , and the projection \mathbf{P}_Π of a contact are objective quantities.

As, on principle, the intergranular force \vec{f} is an objective vector, $f_N = \vec{f} \cdot \vec{n}$ is an objective scalar and consequently, and $\vec{f}_T = \vec{f} - f_N \vec{n}$ is an objective vector. Moreover, as the constitutive equation (Equation 4) for f_N is obviously frame invariant, it ensues that the frame invariance of the constitutive law of the contact force is equivalent to that of the tangential force. The frame invariance of the constitutive law of the tangential force, which is path dependent, cannot be checked directly; however, it can be proven that it comes down to that of the incremental form of the law. The explicit incremental constitutive law for \vec{f}_T can be extracted from the set of equations (Equation 5) that can be seen as a problem for which the data are f_N , \vec{f}_T , \vec{V}_T^r , $\vec{\omega}^n$, and $\vec{\omega}^m$ and the unknowns $\dot{\vec{f}}_T$ and λ , but it is not necessary to make the incremental law explicit. It is enough to show that the set of equations (Equation 5) remains unchanged in a change of frames. To make that verification easier, Equation 5c, taking into account the relation $\dot{\vec{f}}_T \cdot \vec{n} + \vec{f}_T \cdot \dot{\vec{n}} = 0$, is written as follows:

$$\overset{\circ}{\vec{f}}_T = k_T \left(\vec{V}_T^r - \lambda \vec{f}_T \right), \quad 0 \leq \lambda, \quad (8)$$

where

$$\overset{\circ}{\vec{f}}_T = \dot{\vec{f}}_T + (\vec{f}_T \cdot \dot{\vec{n}}) \vec{n} - P_{\Pi} \cdot \frac{1}{2} (\vec{\omega}^n + \vec{\omega}^m) \wedge \vec{f}_T. \quad (9)$$

As \vec{F}_T and f_N are objective quantities, the expression $\|\vec{f}_T\| + \mu f_N$ is frame invariant. Consequently, the frame invariance of the equations (Equation 5) comes down to that of Equation 5c (it has to be noticed that in Equation 5a, because of the nullity of f_N and of $\dot{\vec{f}}_T$, $\dot{\vec{f}}_T = \overset{\circ}{\vec{f}}_T$). As for the frame invariance of Equation 5c, it relies on the two following results: The relative velocity of the grains \vec{V}^r (Equation 6) is an objective vector and $\overset{\circ}{\vec{f}}_T$ of Equation 9 is an objective derivative of \vec{f}_T . The proof of those two results is given in Appendix A.

2.3.3 | Integration of the contact law on a time step

The DEM computation consists in numerically integrating the dynamics equations of the motion of the grains of the elementary cell, the unknowns of the numerical integration being the positions and rotations of the grains, and their velocities of translation and rotation. This is performed using a time stepping method. The dynamical equations involve the contact forces; the normal parts of which are directly given by Equation 4, but their tangential parts are given in the incremental form (Equation 5); it is necessary to integrate this problem in some way to yield a tangential force \vec{f}_T^f at the end of the step in terms of the geometry and the kinematics of the grains making contact at the end of the step. According to Equation 5a, if $f_N^f = 0$, then $\vec{f}_T^f = 0$. It remains to determine \vec{f}_T^f in the case of $f_N^f < 0$, for that $\dot{\vec{f}}_T$ is approximated by the finite difference $(\vec{f}_T^f - \vec{f}_T^i)/\delta t$ where \vec{f}_T^i is the value of \vec{f}_T at the beginning of the step and δt the step length and the left-hand side $P_{\Pi} \cdot \dot{\vec{f}}_T$ of Equation 7 is approximated by $(\vec{f}_T^f - P_{\Pi^f} \cdot \vec{f}_T^i)/\delta t$. Different integration schemes may be considered; a fully implicit scheme and a so-called semiexplicit one with a variant of the approximation of $P_{\Pi} \cdot \dot{\vec{f}}_T$ are presented below.

Semiexplicit scheme

In the semiexplicit scheme, Equation 5c is approximated by the following:

$$(1 + \delta t k_T \lambda^f) \vec{f}_T^f = \vec{f}_T^{fe}, \quad (10)$$

where $\vec{f}_T^{fe} = P_{\Pi^f} \cdot \vec{f}_T^i + \delta t C_N^f \vec{n}^f \wedge \vec{f}_T^i + \delta t k_T \vec{V}_T^{rf}$ is the solution corresponding to an elastic step that is to say to $\lambda^f = 0$. It may be noticed that \vec{f}_T^i is the tangential force at the beginning of the step and that in general the projection $P_{\Pi^f} \cdot \vec{f}_T^i$ of \vec{f}_T^i on Π^f is not \vec{f}_T^i .

The step is elastic and \vec{f}_T^{fe} is the solution if $\|\vec{f}_T^{fe}\| \leq -\mu f_N^f$ (in the case $f_N^f < 0$). Otherwise, if $-\mu f_N^f < \|\vec{f}_T^{fe}\|$, the step is plastic and \vec{f}_T^f has to be such that $\|\vec{f}_T^f\| = -\mu f_N^f$, which yields $1 + \delta t k_T \lambda^f = \|\vec{f}_T^{fe}\| / (-\mu f_N^f)$ and $\vec{f}_T^f = -\mu f_N^f (\vec{f}_T^{fe} / \|\vec{f}_T^{fe}\|)$, that comes down to reduce \vec{f}_T^{fe} to a vector of norm $-\mu f_N^f$. The two cases elastic and plastic can be gathered together by setting $\delta t k_T \lambda^f = (A + |A|)/1$ with $A = \|\vec{f}_T^{fe}\| / (-\mu f_N^f) - 1$.

A variant of this semiexplicit scheme consists in approximating $P_{\Pi} \cdot \dot{\vec{f}}_T$ of Equation 7 by $P_{\Pi} \cdot \dot{\vec{f}}_T \simeq (\vec{f}_T^f - (\mathbb{I} - \vec{n}^i \otimes \vec{n}^f) \cdot \vec{f}_T^i) / \delta t$ instead of $(\vec{f}_T^f - (\mathbb{I} - \vec{n}^f \otimes \vec{n}^f) \cdot \vec{f}_T^i) / \delta t$. In that case, Equation 10 is the same with

$$\vec{f}_T^{fe} = (\mathbb{I} - \vec{n}^i \otimes \vec{n}^f) \cdot \vec{f}_T^i + \delta t C_N^f \vec{n}^f \wedge \vec{f}_T^i + \delta t k_T \vec{V}_T^{rf}. \quad (11)$$

It is that scheme that is used in the numerical implementation used in this paper.

Fully implicit scheme

In the fully implicit scheme, Equations 5b, 7, and 5d are written at the end of the step. Therefore, Equation 7 reads as follows:

$$(1 + \delta t k_T \lambda^f) \vec{f}_T^f - \delta t C_N^f \vec{n}^f \wedge \vec{f}_T^f = \vec{\Phi}^f, \quad (12)$$

where $\vec{\phi}^f = \mathbf{P}_{\Pi^f} \cdot \vec{f}_T^i + \delta t k_T \vec{V}_T^{rf}$. As for the semiexplicit scheme, the expression of \vec{f}_T^f can be obtained in a closed form as follows.

In the considered case of $f_N^f < 0$, the Coulomb condition $\|\vec{f}_T^{fe}\| \leq -\mu f_N^f$ is equivalent to $\|\vec{f}_T^f\|^2 \leq \mu^2(f_N^f)^2$; therefore, in order to determine whether the step is elastic ($\lambda^f = 0$) or plastic ($0 < \lambda^f$), it is necessary to evaluate $\|\vec{f}_T^f\|^2$. The vectors \vec{f}_T^f and $\vec{n}^f \wedge \vec{f}_T^f$ are orthogonal and their norms are equal, and then the taking of the norm of Equation 12 yields the following:

$$\|\vec{f}_T^f\|^2 = \frac{1 + (\delta t C_N^f)^2}{(1 + \delta t k_T \lambda^f)^2 + (\delta t C_N^f)^2} \|\vec{f}_T^{fe}\|^2,$$

where the elastic tangential force \vec{f}_T^{fe} corresponds to $\lambda^f = 0$. An analysis analogous to that of the semiexplicit scheme leads to an expression that gathers together the two occurrences, elastic for $\|\vec{f}_T^{fe}\|^2 \leq \mu^2(f_N^f)^2$ and plastic for $\|\vec{f}_T^{fe}\|^2 > \mu^2(f_N^f)^2$, namely,

$$1 + \delta t k_T \lambda^f = \sqrt{1 + \frac{A + |A|}{2}} \quad \text{where } A = \left(1 + (\delta t C_N^f)^2\right) \left(\frac{\|\vec{f}_T^{fe}\|^2}{\mu^2(f_N^f)^2} - 1 \right).$$

It remains to solve Equation 12 in order to determine \vec{f}_T^f . That can be done by combining Equation 12 and its vectorial product by \vec{n}^f , that yields as follows:

$$\left((1 + \delta t k_T \lambda^f)^2 + (\delta t C_N^f)^2 \right) \vec{f}_T^f = (1 + \delta t k_T \lambda^f) \vec{\Phi}^f + \delta t C_N^f \vec{n}^f \wedge \vec{\Phi}^f.$$

2.4 | Numerical implementation of a DEM-based NHL

In this section, a focus is made on the actual implementation of what was addressed in the previous section. As already stated, periodic boundary conditions (PBCs) are adopted to implement the DEM-based NHL.

A specificity of the DEM is to consider the motion and interaction of each rigid particle that constitutes a granular material. The kinematics of a particle can thus be given by its mass properties, position \vec{r} , velocity \vec{v} , and acceleration \vec{a} , and the time integration can be performed, for instance, by means of the Gear predictor-corrector or the velocity Verlet scheme.³⁴ We may consider a volume element of granular material, which is a parallelepiped and includes a given number of particles. This volume (referred to as *cell* in the present section, or equivalently EV in other parts of the paper) can be defined by three non-collinear vectors as shown in Figure 4, and it can be associated with an operator \mathbf{h} given by a three-by-three matrix defined with the vectors arranged in columns.

Thanks to the matrix \mathbf{h} , the particle kinematics can be expressed in terms of reduced values, namely, the coordinate \vec{s} , the velocity \vec{v} , and the acceleration \vec{a} . They read as a function of reduced kinematics as follows:

$$\vec{r} = \mathbf{h} \cdot \vec{s}, \quad (13)$$

$$\vec{v} = \dot{\mathbf{h}} \cdot \vec{s} + \mathbf{h} \cdot \dot{\vec{s}}, \quad (14)$$

$$\vec{a} = \ddot{\mathbf{h}} \cdot \vec{s} + 2\dot{\mathbf{h}} \cdot \dot{\vec{s}} + \mathbf{h} \cdot \ddot{\vec{s}}, \quad (15)$$

where \vec{s} is the reduced position of a particle and the number of overdots denote for the number of time derivatives. In practice, the reduced acceleration can be simplified in the case of a quasi-static transformation of the cell by $\vec{a} \approx \mathbf{h} \cdot \ddot{\vec{s}}$, which allows for reducing some computations. It may be noticed that \mathbf{h} can be interpreted as the support of a pattern that is infinitely replicated but also as the variable that hold the *collective degrees of freedom* (CDF) of the simulated system. From this point of view, a mass should be given to the CDF so that it is used in the “collective integration” (just like a

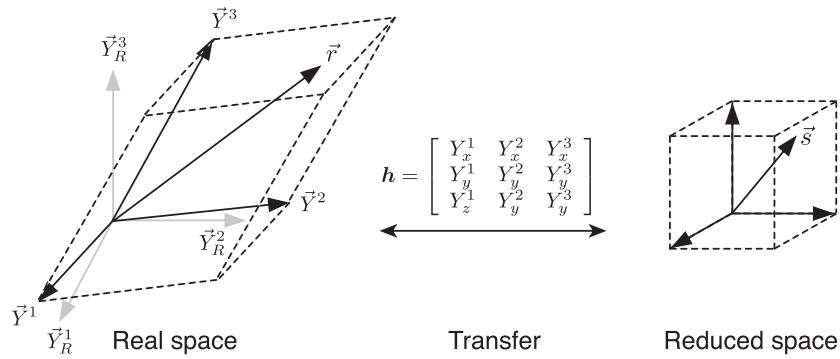


FIGURE 4 Definition of a periodic cell (ie, the simulation domain for the DEM problem) which is a 3D parallelogram parameterised by three vectors. An operator \mathbf{h} allows for the transfer from a real towards a reduced coordinate system $\vec{r} = \mathbf{h} \cdot \vec{s}$, or for the opposite way $\vec{s} = \mathbf{h}^{-1} \cdot \vec{r}$. The reduced space benefits from being an orthonormal coordinate system with position values ranging from 0 to 1. The positions in the real space have their origin at one corner for convenience

classical particle) when a stress is imposed; however, for the two-scale concurrent DEM×FEM coupling, only the stress response caused by an increment of transformation is needed. For this specific application, the time integration of \mathbf{h} is simply performed by imposing a transformation at constant velocity $\dot{\mathbf{h}}$ – and the same integration scheme as the one used for particles is employed. This direct integration avoids the need for supplementary explanations on how to account for an imposed stress component. The interested reader may refer to Radjai et al³⁵ for understanding how to impose stress to a periodic cell. The evolution of \mathbf{h} spans the particle kinematics together with the forces acting in-between the particles that stand inside the same cell or at the boundaries of adjacent cells in the infinite space; it is the core of the PBC. Apart from that, the discrete element method employed is classical, and so are the force laws—provided that the local kinematic parameters (overlap and relative velocities) are expressed in the nonreduced (real) space. It is interesting to underline how the velocity field in the real space can be split into two components: the affine velocity-field \mathbf{hs} and the velocity-fluctuations $\mathbf{h}\vec{s}$, which is a typical feature of discontinuous matters.^{36,37}

The relation between the deformation gradient \mathbf{F} and the evolution of \mathbf{h} can be formalised by expressing the displacement gradient $\nabla_{i \rightarrow f} \mathbf{u}$ from an initial i to a final f state, which can be expressed as $\mathbf{F}^f \cdot (\mathbf{F}^i)^{-1} - \mathbb{I}$:

$$\nabla_{i \rightarrow f} \mathbf{u} = (\mathbf{h}^f - \mathbf{h}^i) \cdot (\mathbf{h}^i)^{-1}, \quad (16)$$

where the idea is to take the state i as a reference instead of the actual reference state.

It must be noticed that, because of the dynamic nature of the DEM, a duration τ needs to be introduced to deform the periodic cell at constant velocity $\dot{\mathbf{h}} = (\nabla_{i \rightarrow f} \mathbf{u} \cdot \mathbf{h}^i)/\tau$. To define this duration and ensure a quasi-static deformation, we can rely on the inertial number I , which is a dimensionless quantity that measures the ratio of inertial to imposed strain times.^{38,39} It is generally accepted that a value lower than 10^{-3} provides a quasi-static regime in DEM simulations. The definition of I involves the maximum rate of shear strain $\dot{\gamma} \equiv \gamma/\tau$, where γ can be estimated from $\nabla_{i \rightarrow f} \mathbf{u}$ with the following relations:

$$\gamma = e_1 - e_3 \quad \text{with} \quad \mathbf{e} = \frac{1}{2}(\nabla_{i \rightarrow f} \mathbf{u} + \nabla_{i \rightarrow f} \mathbf{u}^T), \quad (17)$$

where $e_1 \geq e_2 \geq e_3$ are the eigenvalues of the $i \rightarrow f$ strain \mathbf{e} . It may be noticed that the second-order terms of the finite strain tensor \mathbf{e} has been neglected; this assumption has no consequence on the double-scale modelling itself since the sole purpose of the estimate of γ is to assess the duration τ required by the DEM, and the displacement gradient is not intended to be too large over a single loading increment.

Starting from the definition of the inertial number $I = (\dot{\gamma}\langle d \rangle)/(\sqrt{P/\rho})$, where $\langle d \rangle$ is the average particle diameter, $P = \text{tr}\sigma/3$ is the mean pressure, and ρ is the density of the granular material; the duration τ and consequently the imposed velocity $\dot{\mathbf{h}}$ for the cell transformation can take this form:

$$\tau = \frac{\gamma \langle d \rangle}{I \sqrt{P^i / \rho^i}} \quad \Rightarrow \quad \dot{\mathbf{h}} = \left(\frac{I \sqrt{P^i / \rho^i}}{\gamma \langle d \rangle} \right) \nabla_{i \rightarrow f} \mathbf{u} \cdot \mathbf{h}^i, \quad (18)$$

where the inertial number has been set to $I = 10^{-4}$ in the results presented in this paper. In fact, we need to keep in mind that the determination of τ is only a matter of choice that aims to limit the naturally dynamic response of the DEM. Finally, setting $\dot{\mathbf{h}}$ as a constant value in the DEM computation realises what is expressed in Equation 3.

When the final deformation gradient is reached after a time τ , the static balance has to be satisfied. The deformation gradient \mathbf{F}^f is thus kept the same as long as a criterion is not satisfied with a given tolerance. To define this criterion, we may rely on a normalised relative deviation in the static balance of all particles:

$$\Delta_n < \varepsilon_R \quad \forall n, \quad \text{with} \quad \Delta_n = \frac{\left\| \sum_{m \neq n} \vec{f}^{m/n} \right\|}{\max \left\| \vec{f}^{m/n} \right\|}, \quad (19)$$

where a typical tolerance is $\varepsilon_R = 10^{-3}$. It must however be said that this criterion is drastic and may lead to heavily extended periods of stabilisation. In some cases, a more permissive condition may be necessary, which might be to consider a given tolerance on the cell homogenised pressure for a given number of time steps.

2.4.1 | Implementation of an objective contact force-law with Coulomb friction

This section gives some clarifications about the implementation of a force law as depicted in Section 2.3.3 in the context of periodic boundary conditions. As usual in DEM computations, the forces-laws are expressed in the nonreduced space as functions of local kinematic parameters. Here, they need to be defined in the context of PBCs. First, the branch vector \vec{b} linking the centre of touching particles n and m (see Figure 3) can be assessed that way:

$$\vec{b} = \mathbf{h} \cdot \vec{S} \quad \text{with} \quad \vec{S} = \vec{s}^m - \vec{s}^n - \vec{R}(\vec{s}^m - \vec{s}^n). \quad (20)$$

The operator $\vec{R}(\vec{x})$ rounds each component of \vec{x} to the closest integer; achievable values are therefore -1 , 0 , or 1 . It is a genuine trick to manage the periodicity for boundary particles by taking advantage of the configuration of the reduced space. Figure 5 provides an illustration of the determination of the branch vector between a particle and the image of another particle obtained by translations along the periodic axis. Since each pair of particle is tested with $n < m$, they can be counted only one time.

From the branch vector, the contact normal \vec{n} and the normal overlap d are easily definable. The relative velocity is obtained as follows:

$$\vec{V}^r = (\mathbf{h} \cdot \dot{\vec{S}} + \mathbf{h} \cdot \vec{S}) - (R^n \vec{n} \wedge \vec{\omega}^n + R^m \vec{n} \wedge \vec{\omega}^m) \quad \text{with} \quad \dot{\vec{S}} = \dot{\vec{s}}^m - \dot{\vec{s}}^n. \quad (21)$$

It is important to remark here that fluctuation velocities $\mathbf{h} \cdot \dot{\vec{s}}$ and angular velocities $\vec{\omega}$ are periodic, while affine velocities $\mathbf{h} \cdot \vec{s}$ are *not* periodic. This is implicitly accounted for in Equation 21, thanks to the definition of the vector \vec{S} in the reduced space; see Equation 20.

During explicit-time integration of the particle movements, at a given time increment k , the contact force-laws can be expressed from these local kinematic parameters by means of two functions relying on the normal and tangential components: $\vec{f}^f = f_N^f \vec{n}^f + \vec{f}_T^f$. As a convention, this force expresses the action of particle m on particle n . The normal

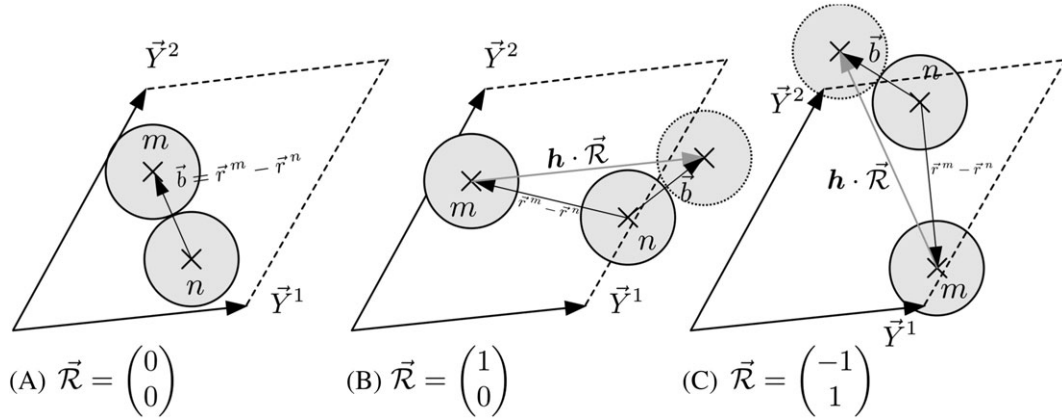


FIGURE 5 Three illustrative cases for the determination of the branch vector \vec{b} from a particle n to an image of the particle m in a 2D real space: (A) case of two particles standing within the cell, the image of m is m itself; (B) case where the image of m is obtained by a translation $\vec{Y}^2 - \vec{Y}^1$; (C) case where the image of m is obtained by a translation $\vec{Y}^2 - \vec{Y}^1$.

force is given by the following:

$$f_N^f = k_N d^f + 2\eta \sqrt{k_N \frac{M^m + M^n}{M^m M^n}} (\vec{V}^{rf} \cdot \vec{n}^f), \quad \eta \in [0; 1[, \quad (22)$$

where η is a viscous damping rate that aims mainly to damp the energy and to improve the numerical stability and M denotes the particle masses. It is also possible to damp numerically the whole system by using the solution employed in PFC, which is not physical but acceptable in case of slow transformations.

For the tangential component of the force, an increment of relative displacement is considered. This vector stands in the plan Π of contact accumulated within a single integration time-step δt , and in the context of an time-explicit integration scheme, it is approximated by

$$\Delta \vec{u}_T^f = \delta t (\mathbf{P}_\Pi \cdot \vec{V}^{rf}) = \delta t \left(\vec{V}^{rf} - (\vec{V}^{rf} \cdot \vec{n}^f) \vec{n}^f \right). \quad (23)$$

The tangential component of the force that involves irreversible displacements is then computed incrementally at each time step according to the semiexplicit scheme depicted in Section 2.3.3:

$$\vec{f}_{T,\text{trial}}^f = (\mathbb{I} - \vec{n}^i \otimes \vec{n}^f) \cdot \vec{f}_T^i + \delta t C_N^f \vec{n}^f \wedge \vec{f}_T^i + k_T \Delta \vec{u}_T^f \quad (24)$$

$$= \vec{f}_T^i - \vec{f}_T^i \wedge (\vec{n}^i \wedge \vec{n}^f) + \left(\left(\frac{(\vec{\omega}^{nf} + \vec{\omega}^{mf})}{2} \cdot \vec{n}^f \right) \vec{n}^f \right) \wedge \vec{f}_T^i + k_T \Delta \vec{u}_T^f. \quad (25)$$

In this expression, the first term may be interpreted as a correction that accounts for the rotation of the tangent plane, and the second term corrects the rotations of the particles.

Finally, this trial force is explicitly cut to its maximum magnitude according to the Coulomb friction condition:

$$\vec{f}_T^f = \begin{cases} \vec{f}_{T,\text{trial}}^f & \text{if } \|\vec{f}_{T,\text{trial}}^f\| < \mu \langle f_N \rangle_+ \\ (\mu \langle f_N \rangle_+) \frac{\vec{f}_{T,\text{trial}}^f}{\|\vec{f}_{T,\text{trial}}^f\|} & \text{otherwise,} \end{cases} \quad (26)$$

where μ is the Coulomb coefficient of friction, taken as a constant here, and $\langle f_N \rangle_+$ is f_N excepted that it equals 0 if f_N is negative (this can happen due to the added normal viscosity).

Here, we considered only purely frictional contacts like in dry sands or frictional-cohesive contacts like in unsaturated sands. There is actually no limitation in the complexity at the DEM level (definition of DEM force laws, polyhedral shapes, etc.). Indeed, a more advanced frictional-cemented law (not presented in this paper) for the modelling of sandstones has also been developed.

2.4.2 | Numerical homogenisation procedure

At the FEM scale (Gauss points), a constitutive equation has to provide the Cauchy stress as a function \mathcal{S} of the transformation gradients as expressed in Equation 1. This job can be handled by the DEM computation by using PBC. In this case, the mechanical response of the DEM cell will play the role of a constitutive laws, which is actually a Numerically Homogenised Law (NHL). The numerical homogenisation allows for the assessment of the average stress tensor, and it is performed, thanks to the Cauchy-Poisson relation:

$$\boldsymbol{\sigma} = \frac{1}{V} \sum_n \sum_{m>n} \vec{f}^{m/n} \otimes \vec{b}^{mn}, \quad (27)$$

where $V = |\det \mathbf{h}|$ is the volume of the cell; (n, m) denotes the contact that involves the particles n and m ; $\vec{f}^{m/n}$ is the total (normal and tangential) action of the particle m on n ; and \vec{b}^{mn} is the branch vector defined in Equation 20. It is worth noting that Equation 27 continues to be valid whatever the physical cause and the dimension of the forces involved; but it includes no dynamic contribution and thus requires a quasi-static state of the particles in order to be substantiated.

In the end, the NHL is established by (1) the PBC (Section 2.4), (2) a right choice of straining rate (Equation 18), (3) a criterion to ensure a quasi-static equilibrium (eg, Equation 19), and (4) a relation to numerically perform an homogenisation to assess the mean stress tensor (Equation 27). With these ingredients, the NHL part of the principle diagram depicted in Figure 1 can seamlessly be implemented. However, a tricky question arises: What is the right size, in terms of number of particles, for an elementary cell? This question is difficult to address because the cell is meant to be representative of

the behaviour of the granular material to be modelled. However, an increase in the amount of particles favours the strain localisation within the periodic cell, which is somehow in conflict with the need of “representativeness.” In actual fact, too few or too much particles will provide inadequate global responses, and an operable amount is found to be in the order of one thousand particles in 3D DEM and of a few hundred particles in 2D DEM—that is only one to two 10th particles per side. This uncomfortable situation can be dealt with by regarding the periodic cell as kinematic data required by a NHL and *not* as a piece of laboratory specimen.

2.5 | Building a FEM quasi-Newton robust operator

2.5.1 | Link with classical geomechanics FEM codes

As presented in Section 2.2, the non-linear macroscopic boundary-value problem consisting of Equation 2 and of the constitutive law Equation 1, which, in this work, is the NHL law, is solved using a Newton-Raphson or a quasi-Newton-Raphson method. Equations are expanded up to the first order with respect to the unknowns, ie, the displacement field from Ω^i to Ω^f , the stress σ^f , and the appropriate parts of \vec{F}^f . At each iteration, the resulting linear system is solved and the unknowns are updated. In those methods, a linear relation yielding the increment $d\sigma^f$ as a linear function of the increment $d\mathbf{F}^f$ is needed:

$$d\sigma^f = C : d\mathbf{F}^f. \quad (28)$$

In the actual Newton-Raphson method, which is known to yield the highest convergence rate, the previous relation is provided by the differentiation of the integrated constitutive law Equation 1. The resulting operator is called the consistent tangent operator (CTO) and denoted by C^{CTO} :

$$d\sigma^f = S(\mathbf{F}^f + d\mathbf{F}^f) - S(\mathbf{F}^f) = C^{CTO} : d\mathbf{F}^f + \dots . \quad (29)$$

In most of the cases, particularly in the present one, the determination of C is performed numerically by a perturbation method. For a 3D problem, \mathbf{F}^f is perturbed in nine independent directions, for instance, given by the nine second-order tensors Λ^{nm} , $n, m = 1, 2, 3$ such that

$$\Lambda_{kl}^{mn} = \delta_{mk}\delta_{nl}, \quad (30)$$

where δ is the Kronecker symbol. The components of the C^{CTO} are then computed by the following:

$$C_{ijmn}^{CTO} = \frac{S_{ij}(\mathbf{F}^f + \epsilon\Lambda^{mn}) - S_{ij}(\mathbf{F}^f)}{\epsilon}, \quad (31)$$

where ϵ is a suitably chosen small number.

It is worth noticing that S has to be evaluated 10 times at each iteration of the Newton-Raphson method, once for the computation of $S_{ij}(\mathbf{F}^f)$ and the other nine times for the computations of $S_{ij}(\mathbf{F}^f + \epsilon\Lambda^{mn})$. That is a really time-consuming task, particularly in the case of the NHL since, because of Equation 3, each evaluation of S consists in a DEM computation along a slightly different but equivalently long deformation path. Because of the inevitably noisy response of DEM computations in the postpeak regime, poorly defined numerical derivation of the tangent operator is obtained, leading to a bad convergence of the Newton-Raphson iterative process, or no convergence at all. In addition, the time required to perform each of the DEM computations involved in the perturbation process creates an important overhead that results in a consequent computational time at the upper scale BVP level. This is the reason why different alternative methods to obtain substitute C operators are proposed.

2.5.2 | Alternative substitute operators

The aim is to find a candidate that gives better stability and convergence rates, if possible at lower CPU cost. A total of eight operators have been studied, including the consistent one. Those operators are divided into three groups: perturbation based, Kruyt-type, and elastic. In the sequel, the operators are briefly described, and more detailed descriptions can be found in Argilaga et al.³¹

Perturbation-based operators

While the previously defined CTO consists in the perturbation technique defined by Equations 30 and 31, an auxiliary elastic operator (AEO) can be defined using the perturbation technique only for the steps performed in the strain-hardening regime of the material's behaviour, referred to as strain regime I in Roux et al.⁴⁰ When entering the peak and postpeak

regime, the AEO operator is defined as the average of the CTOs obtained in the prepeak regime and kept constant in the sequel of the computation.

Kruyt operators

Kruyt operators constitute a more simplistic homogenisation technique that considers that the displacements and rotations of the grains are equal to the ones of the macroscopic field. The upper bound Kruyt operator (UKO) is based on Kruyt et al⁴¹ and the upper bound corrected Kruyt with two calibration coefficients have been proposed (UCKO 2 DOF). A variation of Kruyt-based operators can also be proposed by adding additional degrees of freedom, such as the prestresses and rotation of grains, thus obtaining the augmented Kruyt operator (KAO).

Elastic operators

Elastic operators consist in computing an elastic equivalent stiffness of the DEM assembly. The prestressed truss-like operator (PSTLO) considers the DEM assembly to behave like a static truss structure rather than a dynamic granular media, still taking into account the rotational degrees of freedom of the grains and the prestresses. The advantage of this method is that it allows to obtain the elastic coefficients directly, providing the resolution of a linear system.

Alternatively, the DEM quasi-elastic (DEMQO) can be defined as the numerical version of the PSTLO. Instead of building a global stiffness matrix that represents the DEM contact network, DEMQO uses the DEM code itself with additional conditions to render it quasi-elastic, ie, impose very high contact friction that prevents the grains to slide inelastically. Then the coefficients can be obtained with a modified, much less CPU-demanding perturbation-like method that consists in soliciting the DEM computation after the considered time step for the deformation gradients $\mathbf{F}^f + \epsilon \Lambda^{mn}$, $m, n = 1, 2, 3$ with \mathbf{F}^f as the starting point of the computation, as if it was a new time step. The corresponding operator then reads as follows:

$$C_{ijmn}^{\text{DEMQO}} = \frac{S_{ij}^E(\mathbf{F}^f + \epsilon \Lambda^{mn}) - S_{ij}(\mathbf{F}^f)}{\epsilon}, \quad (32)$$

where S_{ij}^E is the NHL corresponding to this complementary time step, while S_{ij} is the same as in Equation 31.

It turns out that the DEMQO procedure results in an important computational time reduction with respect to PSTLO, and to CTO as well, as expected for the latter.

2.5.3 | Compared efficiency of the operators

A numerical study based on a 128 eight-noded plane strain elements with 4 Gauss points FEM mesh to model a biaxial test with constant lateral pressure and axial shortening at constant rate was performed. The microscale model was using 2D DEM 20×20 grains elementary volumes. Figure 6 shows the convergence performances of the operators in the initial stage of the compression and after the stress peak. It displays the number of iterations needed to reach convergence with a precision threshold $|F|/|R| = 10^{-3}$ in the initial part of the computation (up to the peak and somewhat after) and $|F|/|R| = 10^{-2}$ after the peak,* where $|F|$ is the norm of the nodal forces and $|R|$ is the norm of the nodal reactions in the current iteration. These results show that the best overall performance is obtained with DEMQO/PSTLO. In the case of the perturbation-based operators, the CTO is shown for the initial part and the AEO for the postpeak since the CTO does not work in the postpeak and the AEO is the CTO in the initial part. In the case of the UCKO and UCKO 2 DOF, the calibration improves the performance in the initial stages with respect to the non calibrated UKO; this is because the proposed calibration is performed with the CTO at the beginning of the loading (CTO being non-available later). Finally, the convergence improvement efficiency of the AEO with respect to the UKO is significant in the initial part but not much in the postpeak. Table 1 summarises the properties of the different operators, and references are provided.

As for the UCKO-like operators, it should be mentioned that they require a calibration phase that is not here considered and that can be hardly extended to different problems. The KAO, which accounts for rotations pre-existing forces in the microscale, proves to be an enhancement of the original UKO but limited to the prepeak regime. Finally, it is worth noting that the DEMQO offers the most interesting performances both in terms of number of iterations and total wall-clock time. The here proposed approach is indeed 35% more efficient than the commonly adopted Kruyt operator.

*When strain localisation develops, inducing strong non-linearities in the NHL constitutive law, convergence stops progressing after a few iterations in the Newton-Raphson loop. This leads to alleviate the convergence criterion at 10^{-2} in postpeak steps.

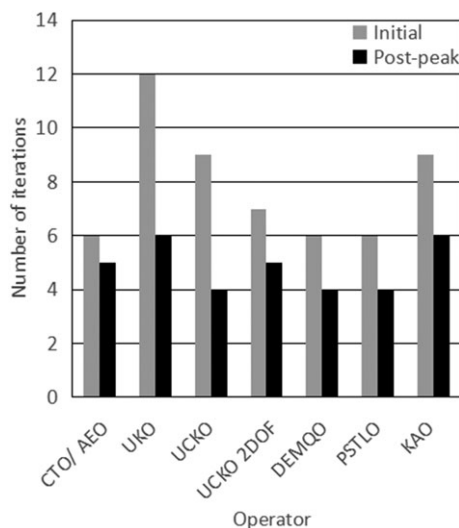


FIGURE 6 Number of iterations needed to reach convergence with the different operators. The convergence threshold in the postpeak regime is 1% of norm of forces over the norm of reactions

TABLE 1 Summary operators^a

Operator	Advantages	Disadvantages	V_i	V_p	References
CTO	Quadratic	Perturbations	0.20	—	Equation 31; Simo et al ⁴²
AEO	No perturbations	Not updated	0.20	0.80	Nguyen et al ⁴³
DEMQO	Robust, fast	Numerical	1.00	1.00	Equation 32
PSTLO	Robust, fast	System solver	1.00	1.00	Argilaga et al ³¹
UKO	Simple computation	Not physical	0.50	0.67	Kruyt et al ⁴¹
UCKO	Better fit	Not physical	0.67	1.00	Argilaga et al ³¹
UCKO 2DOF	Yet better fit	Not physical	0.86	0.80	Argilaga et al ³¹
KAO	Considers rotations	Not physical	0.67	0.67	Argilaga et al ³¹

^aThe convergence velocity is computed as the inverse of the number of integrations of the loading path, both for the initial stages (V_i) and postpeak (V_p), and the values are normalised with the reference of the DEMQO/PSTLO. Note that in the perturbation-based methods, the number of needed integrations is five for each iteration.

2.6 | Enhancing the 2D microscale DEM model to 3D

2D granular materials are essentially academic materials whose experimental realisations, made of disks lying on their large faces on a smooth lubricated plane, or rods piled up along their generatrices,^{44,45} have been created for fundamental studies of simplified granular media or to assess schematically some kinematical hypothesis of localised rupture modes in model tests of, eg, retaining walls.⁴⁶ In the real world, grains are 3D objects. The differences between the behaviours of assemblies of 2D and 3D grains are very significant: 2D grain assemblies have much less adjustment opportunities when subjected to an overall deformation process, leading, eg, to much smaller void ratio variation range. 3D grain assemblies studied using DEM behave in a much more realistic way with respect to real granular media. Among other features, even in plane strain problems, their response depends not only on the in-plane stress tensor but also on the out-of-plane stress components.

It may be expected that modelling 3D EVs of grains would require much more grains in 3D than in 2D. In fact, the increase of grain number from the 2D case to the 3D to obtain a reasonably representative response for a 3D EV is not that large that it could be expected: typically, a volume of at least $20 \times 20 = 400$ grains was found to be necessary for deriving an NHL in 2D in Guo et al and Nguyen^{20,43} while $10 \times 10 \times 10 = 1000$ spherical grains turn out to be good enough in 3D.³⁰ In the FEM×DEM framework, the NHL obtained using 3D DEM will be more physically representative of real materials like sand; it will take into account the 3D stress components, which is important not only in 3D macroscopic simulations but also in 2D plane strain or axisymmetric 2D macro problems. Last, it will be shown in Section 6 that in, eg, biaxial test simulations, 3D DEM NHL leads to much more realistic and smoother responses than 2D and allows to follow the tests much further in the postlocalisation regime.

2.6.1 | Kruyt operators in 3D case

In case of 3D micro model coupling with macro-FEM model, instead of the tangent operator defined above, we use an operator extracted from the underlying granular structure of the EV as described in Kruyt et al.^{41,47} Since the relation by Kruyt and Rothenburg is only valid for 2D problem, an extended solution for the 3D case is proposed (Equation 33). It results in the following form of elastic stiffness operator:

$$C_{ijkl} = \frac{1}{V} \sum_{c \in V} (k_n n_i^c b_j^c n_k^c b_l^c + k_t t_i^c b_j^c t_k^c b_l^c + k_w w_i^c b_j^c w_k^c b_l^c), \quad (33)$$

where V is the volume of granular packing. k_n , k_t are normal and tangential contact stiffnesses, respectively; \mathbf{b} is the branch vector connecting two centres of particles in contact; and \mathbf{n} , \mathbf{t} , and \mathbf{w} are three vectors that define the contact forces directions: \mathbf{n} is the normal direction and \mathbf{t} and \mathbf{w} are arbitrarily positioned in the sliding plan so that $\mathbf{w} = \mathbf{n} \wedge \mathbf{t}$.

3 | PARALLEL COMPUTING: TAKING UP THE CPU-TIME COST CHALLENGE

Is concurrent numerical multiscale analysis an attractive but unrealistic dream?

Double-scale integrated model is clearly a highly CPU-time demanding numerical approach. Associating a microscale BVP to each integration point in a macroscale FEM computation requires to solve a number of microscale BVP equal to the number of macroscale elements Nb_{El} times the number of integration point Nb_{IP} in each of those element, for each iteration of each loading step of the macroscale problem. Is it tractable? The answer is YES, providing *high performance computing* (HPC) strategies are used: Parallelisation is the key for practical applicability of multiscale analysis in geomechanics.

In a sequential flow chart, a first estimation of the total CPU cost CPU_t of one macroscale BVP iteration in the Newton-Raphson loop can be stated as $Nb_{El} \times Nb_{IP}$ times the CPU time necessary to solve one microscale BVP CPU_m , plus the time necessary to assemble and solve the macroscale linear system CPU_M :

$$CPU_t = Nb_{El} \times Nb_{IP} \times CPU_m + CPU_M.$$

Of course, this estimate is no longer correct as the computation progresses towards regimes where some elements of the macroscale problem undergo significantly smaller or larger deformation increments than the average. Anyway, based on this estimate, one can state the improved wall-clock time wcT resulting from using concurrently N_{th} computing threads as

$$wcT = \frac{Nb_{El} \times Nb_{IP}}{N_{th}} \times CPU_m + CPU_M + t_{Synch},$$

where t_{Synch} is the extra time cost induced by the synchronisation of the different threads, including communication time between threads and waiting time for, eg, exclusive in turn memory access by the threads, or waiting for one thread to finish a longer than average task.

Depending on the ratios CPU_m/CPU_M and CPU_m/t_{Synch} , the efficiency of the parallelisation can be measured by a scalability factor $ScalF$ defined as

$$ScalF = \frac{1}{n} \frac{wcT(1)}{wcT(n)},$$

which can vary in the range 0% to 100%. Clearly, the efficiency will be very low when a macroscale problem with a very large number of degree of freedom, on the other hand involving a rather simple microscale NHL as, eg, a simple elastic truss. In such a case, most of the time will be spent in solving the macroscale linear system, the gain of time due to parallelising the microscale problems will be negligible and the extra cost due to synchronisation time will not be compensated by any gain. In other words, such problems are “solver intensive.” Conversely, in the case of “heavy,” ie, highly CPU time demanding microscale BVP, the ratios CPU_m/CPU_M and CPU_m/t_{Synch} may become as large as 1 or even more. Most of the total CPU time (summing up the CPU time spent in all the processors) is spent in the element loop, such problems can be said “element-intensive.” This is typically the case of FEM×DEM modelling. In this case, the scalability factor may become pretty good, in the range 50% to 100%, depending on the strategies developed to reduce the synchronisation time t_{Synch} .

3.1 | FEM×DEM method implementation in Lagamine FEM code

The FEM×DEM method was implemented in Lagamine FEM code developed in Liège University.^{48,49} The implementation consisted in incorporating the DEM code as yet another model in the set of constitutive models available in Lagamine. It can be mentioned incidentally here that a FE² double-scale method using FEM at both the macroscale and microscale has been implemented in the same way (see van den Eijnden et al^{5,6}).

Two parallelisation framework has been used in the FEM×DEM studies reported in this paper, namely, OpenMP and MPI parallel computing models. Each of these two models has its own merits and drawbacks: The first model is simpler to implement but limited in number of threads; the second one requires more changes to be made in the host code, but the potential gain is much larger since the number of threads that can be used is not limited.

3.2 | OpenMP parallel computing model

The OpenMP parallel computing model is a Single Program Multiple Data (SPMD) model, based on shared memory computer architecture. In this model, a part of the code is parallelised, which means that this part of code is run simultaneously on several cores, for different data. This is possible only if the computations performed for a given set of data in this part is independent of those performed on another set. Only the results have to be gathered during or at the end of the parallel section, to contribute to the global work flow. OpenMP library offers a set of meta-instructions so-called *parallel directives* allowing to perform safely the gathering task into a shared memory made accessible to all the parallel threads. In a FEM code, the element loop is quite easy to parallelise in this way: Each element is independent of the others, and each of them has to compute and add its own contribution to the global stiffness matrix and force vector. The adding instructions are protected using the “atomic” construct in the OpenMP implementation, which ensures that a specific storage location is updated safely without exposing it to the possibility of multiple, simultaneous writing attempts by several threads.⁵⁰ The OpenMP shared memory parallelisation of the finite element code Lagamine used in this work is presented in Germain⁵¹ and Chambon et al⁵² and illustrated in Figure 7.

3.2.1 | Performances

The performance of the FEM×DEM Lagamine code parallelised using the OpenMP model can be appreciated from Figure 8 and Table 2 where wCT (for wall-clock time) is the measured time for a given simulation . Here, the parallelised

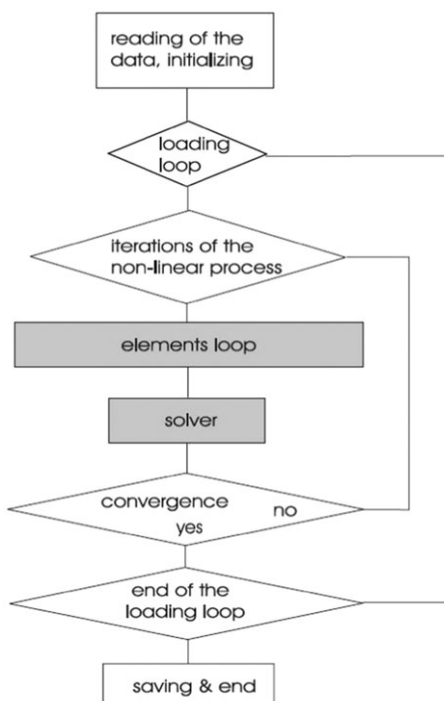


FIGURE 7 LAGAMINE code structure (from Chambon et al⁵²)

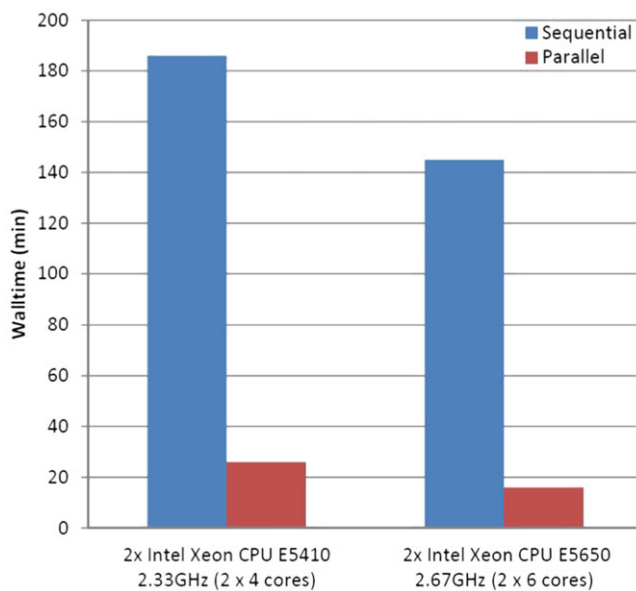


FIGURE 8 Parallelisation performance: comparison of sequential and parallel wall time of a FEMxDEM simulation in different machines [Colour figure can be viewed at wileyonlinelibrary.com]

TABLE 2 Study of the OpenMP scalability factor ScalF as function of the number of shared memory processor cores, measured at the same load

Nb Grains in EV	n Cores	wcT(n), min	$\frac{wcT(1)}{wcT(n)}$	ScalF $= \frac{1}{n} \frac{wcT(1)}{wcT(n)}$
400	1/8	185	1	-
400	8	26	7.15	89%
400	1/12	143	1	-
400	12	16	9.06	76%

code is executed in different machines in order to benchmark its performances. The machines are two servers, one with two Intel Xeon CPU E5410 @2.33GHz 4 core processors (8 cores total) and the second with two Intel Xeon CPU E5650 @2.67GHz 6 core processors (12 cores total). A standard 512-element simulation consisting in a compression biaxial test till 2% of longitudinal strain is executed both sequentially and parallelised in the two machines. The results show a speed-up of 7.15 for the machine with 8 cores and 9.06 for the machine with 12 cores. This is a pretty good result in terms of efficiency of the parallelisation. As mentioned before, the drawback of the OpenMP model is that it cannot use more threads than permitted by the number of memory-sharing cores available on a single computer.

3.3 | MPI parallel computing model

The MPI parallel computing model is a Multiple Program Multiple Data (MPMD) model, using distributed memory rather than shared memory. So it can be deployed on several computers into a cluster or even on several clusters. Consequently, the number of usable threads is not limited. MPI is an acronym for “Message Passing Interface,” it is the name of a model which implements in a standard way the process of dealing with data transfers between completely independent threads running different codes on possibly different computers: typically, a master program (so-called “Boss” afterwards) that sends requests to a set of programs (“Workers” afterwards), which perform a given task and send back a result.

To develop a MPI model version of Lagamine FEM code, the choice has been made to select the lowest elementary task in the element loop of the code: ie, not the element itself, not even the Integration Point, but the call to the constitutive law itself (ie, the DEM code in the present FEMxDEM discussion). This choice implies that the Worker’s code is essentially the DEM code, while the Boss is essentially the Lagamine basic code, yet fitted with a few adjustments described afterwards.

In Lagamine code, constitutive laws are often called in two steps: If the constitutive Law “lawX” is to be used, a first subroutine generically called “Pilot_<lawX>” is called by the element subroutine, and this “Pilot” in turns calls the constitutive law subroutine “lawX.” This procedure allows for example to implement a perturbation loop to derive numerically a consistent tangent operator in a more clear way than including the perturbation loop in the constitutive law code itself. Our MPI parallel model implementation in Lagamine takes advantage of this two-steps calling scheme in the following way: the Pilot generates *requests* which are data sets including all the information to be passed to the constitutive code, posts these *requests* towards the Worker’s team using MPI library tools, and monitors the arrival of *responses* posted by Workers after completion of the work attached to a given request. Figure 9 illustrates this process.

Among the tasks performed in the Element routine for a given integration point (IP) in a standard FEM code, calling the constitutive routine is not the only one: Before that, the strain tensor to be passed to the constitutive routine has to be computed: this is the task “A” presented in Figure 10. Then the call to the constitutive routine allows to get the stress update and the tangent operator: This is the task “B.” Last, the contributions to the global stiffness matrix and to the global Force vector have to be computed using the data returned by the constitutive routine: This is the task “C.” In our MPI version of Lagamine code, tasks A and C are still operated by the master program (Boss), but task B is performed by a separated program, run by one of the workers. The parallelisation consists in having several task B running in separated threads, each for a given IP, because tasks B take considerably more time than A and C. Of course, for a given IP, tasks A, B, and C have to be performed one after the other. As soon as the task A has been performed for a given IP of a given element, any nonoccupied worker can start working on the corresponding task B provided that task A includes the preparation and post of the *request*. But it is essential for the performance of the parallel model that tasks A, B, and C should be completely uncoupled, in such a way that task C for a IP “i” should be performed as soon as task B is finished for this IP (and response data posted by the worker), even though the A-type tasks may have not been already completed for all the IPs. Consequently, in the MPI Lagamine version described here, task “A” includes preparing and posting the *request*, and task “C” includes checking the arrival of responses and retrieving the corresponding data. The circular arrows in Figure 10 aim at stressing this concurrent looping process over tasks A, B, and C. Practically, this means that the element loop in the MPI Lagamine code will be headed by an overlaying loop that will end only after all the tasks “C” have been completed.

In addition, a significant improvement of the efficiency of the parallelisation model relies on a load balancing process settled in the following way: The time spent in each request at the previous iteration of the current loading step is used to build a requests list (element, integration point, and perturbations if any) ordered by decreasing time cost. This list, associated with the introduction of a supplementary program “Supervisor” playing the role of interface between the Boss

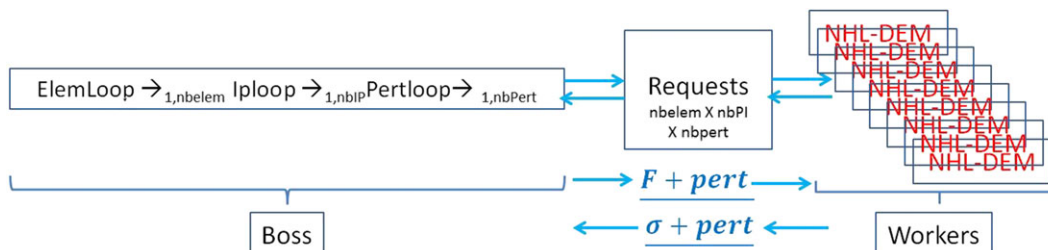


FIGURE 9 Schematic illustration of the message passing architecture used to parallelise the calls to the DEM-based numerical constitutive law NHL-DEM [Colour figure can be viewed at wileyonlinelibrary.com]

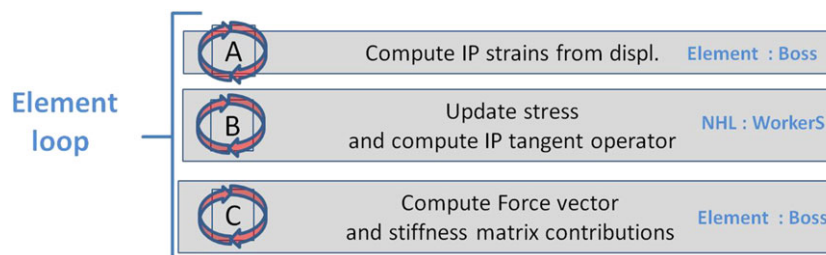


FIGURE 10 Schematic illustration of the message passing architecture used to parallelise the calls to the DEM-based numerical constitutive law NHL-DEM [Colour figure can be viewed at wileyonlinelibrary.com]

TABLE 3 Study of the scalability factor ScalF as function of the number of grains and number of processors, measured at the same load step 30

Nb Grains in EV	n Workers	wcT(n), min	$\frac{wcT(1)}{wcT(n)}$	ScalF $= \frac{1}{n} \frac{wcT(1)}{wcT(n)}$
400	1	172	1	-
400	10	21	8,2	82%
400	50	8	21.5	43%
1600	1	3401	1	-
1600	50	77	44	88%

and the worker's team, allows to process in priority the more time demanding requests, in order to avoid finishing the process with one or a few threads processing long requests while the rest of the worker's team is waiting.

3.3.1 | Performances

Table 3 presents the results of a benchmark realised on a plane strain model of a biaxial test using a 2D FEM mesh of 128 Q8 finite elements with 4 integration points at the macroscale, and 2D DEM elementary volumes of 400 or 1600 circular grains at the microscale. The computations were performed using 1, 10, and 50 workers, on a cluster equipped with Intel Xeon E5-2620@2.00GHz processors with 6 cores and 256GB RAM. The measured time noted wcT in the table is the wall-clock time at the step 30 of the computation, corresponding to a global axial strain = 1.2 % (postpeak regime).

One can conclude that the heavier the microscale problem (large EVs), the better is the scalability: with 50 workers, the scalability factor increases from 43% to 88% when changing the EV size from 400 to 1600 2D grains.

Notwithstanding the improvement of efficiency of the parallelisation (that is what measures the scalability factor), a heavier microscale problem still costs much more than a light one: the total CPU time (wall-clock time) for the “rather heavy” elementary volume with 1600 2D grains is 77 minutes versus 8 minutes for the 400 grains case, ie, the 1600 grains takes about 10 times more time than the 400 grains, which is a huge price to pay for increasing the EV number of grains only by 4.

On the other hand, the parallel run with 50 workers takes 1 hour and 17 minutes instead of 2 days and 8 hours in the sequential case, which is a quite noticeable acceleration of the computation.

The major advantage of the MPI parallelisation model with respect to the OpenMP model is to allow for using a much larger number of threads. The communication overhead may induce a drop of the efficiency for large numbers of threads, this drop is less severe for large DEM elementary volumes. Moreover, different communication modes can be used for passing the large data sets containing the elementary volume data, namely, the grain's positions and contact forces. Changing the communication mode for these data sets from disk file writing to pure message passing reduces significantly the communication overhead but increases drastically the amount of RAM needed for a given computation. Compromises have to be sought out, depending on the applications and the computer resources available.

4 | INTRODUCTION OF AN INTERNAL LENGTH AT THE MACROSCALE

Models using a first-order constitutive relation of classical mechanical continuum cannot properly predict the behaviour of a medium with high strain gradients, for example, problems involving strain localisation: It is well known that for such problems, mesh dependency occurs in the FEM simulations, leading to nonobjectivity of the solutions obtained. An explanation that is commonly put forward is that the first-order constitutive relation does not give any information about an internal length in the model; as a consequence, the localisation band thickness tends to shrink to a size dictated by the mesh size. In this way, if the mesh is refined, the strain will concentrate in a null size band if the size of elements tends to zero.

Based on a continuum approach, several approaches exist in the literature:

- Viscoelastic models introduce rate dependency which introduces, in transitory problems, an internal length; however, in quasi-static problems, the viscous terms do not provide any spatial regularisation.

- Nonlocal models use a space averaging around the material points in order to enrich the constitutive relation with second-order terms; nevertheless, nonlocal models do not obey local action principle and can present conflicts in the boundary of the domain.
- Microstructured local models, based on Mindlin,⁵³ consider a microscale continuum enriched with higher order terms; this is further developed in the following.

In the work presented, a microstructured-like model based on a local second gradient enrichment is chosen. Other microstructured local models could be used alternatively, eg, Cosserats model, that would provide as well a law for the double stresses, independently of the homogenised law (NHL) for the first gradient.

4.1 | Local second gradient model

Microstructured material descriptions consider a continuum field in the microscale enriched by higher order terms.⁵³ In this way, the kinematics of the media is enriched by introducing a local dependency on an internal length parameter. This characteristic length⁵⁴ regularises the solution, making strain localisation mesh independent. A local formulation complies with the principle of local action so it states a stress-strain relationship in the same manner as a classical constitutive laws do, this makes the implementation of local regularisation in classical models a straight forward procedure (Figure 11).

4.2 | Basic equations

4.2.1 | Variational principle

The weak form of the balance equations written for the strain gradient theory is treated as a particular case of the microstructured continuum theory^{53,55,56}:

$$\int_{\Omega^t} \left(\sigma_{ij}^t \frac{\partial u_i^*}{\partial x_j^t} + \Sigma_{ijk}^t \frac{\partial^2 u_i^*}{\partial x_j^t \partial x_k^t} \right) d\Omega^t - \bar{P}_e^r = 0, \quad (34)$$

where, superscripts t and $*$ denote respectively quantities at a given time t and virtual quantities, σ_{ij}^t is the Cauchy stress tensor, Σ_{ijk}^t is the corresponding double stress tensor, u_i^* is a kinematically admissible virtual displacement field, x_i^t are the current coordinates of the points of the studied body, and P_e^* is the external virtual work generated by the corresponding external forces.⁵⁷

Assuming for simplicity that there is no body double force and that the boundary of Ω^t is regular, which means that it is possible to define an external normal in every point of this boundary, the external virtual work reads as follows:

$$\bar{P}_e^* = \int_{\Omega^t} \rho^t f_i^t u_i^* d\Omega^t + \int_{\Gamma_\sigma^t} (p_i^t u_i^* + P_i^t D u_i^*) d\Gamma^t, \quad (35)$$

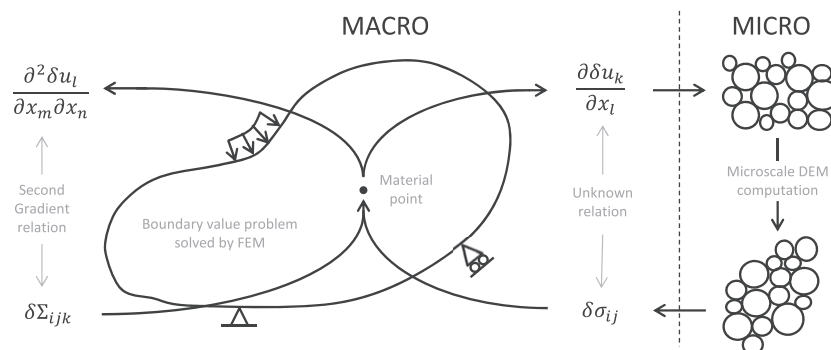


FIGURE 11 FEMxDEM computational homogenisation scheme with local second gradient: the second-order constitutive relation is *independent* from the first-order one, which means that the Cauchy stresses depend only on the first deformation gradient while the double stresses depend only on the second deformation gradient

where f_i^t is the body force per unit mass, ρ^t is the mass density, p_i^t is the external force per unit area, and p_i^t an additional external (double) force per unit area, all applied on a part Γ_σ^t of the boundary Γ^t . D denotes the normal derivative of any quantity q , ($Dq = (\partial q / \partial x_k) n_k$) .

Constitutive equations of second gradient media involve the first and second derivatives of the displacement field and if the first derivative is dimensionless, in contrast the dimension of the second derivative is that of the inverse on a length, consistently introducing a intrinsic characteristic length in the modelling.

4.2.2 | Strong form of the balance equations

As usual, starting by (Equation 34), using the divergence theorem and integrations by parts, allows us to get the strong form of the balance equation in the whole continuum:

$$\frac{\partial \sigma_{ij}^t}{\partial x_j^t} + \frac{\partial^2 \Sigma_{ijk}^t}{\partial x_j^t \partial x_k^t} + \rho^t f_i^t = 0. \quad (36)$$

Similarly, the links between p_i^t, P_i^t and the local values (on the boundaries) of the stress and the double stress can be deduced^{53,55,58}

$$\sigma_{ij}^t n_j^t - n_k^t n_j^t D\Sigma_{ijk}^t - \frac{D\Sigma_{ijk}^t}{Dx_k^t} n_j^t - \frac{D\Sigma_{ijk}^t}{Dx_j^t} n_k^t + \frac{Dn_l^t}{Dx_l^t} \Sigma_{ijk}^t n_j^t n_k^t - \frac{Dn_j^t}{Dx_k^t} \Sigma_{ijk}^t = p_i^t \quad (37)$$

and

$$\Sigma_{ijk}^t n_j^t n_k^t = P_i^t, \quad (38)$$

where Dq/Dx_j denotes the tangential derivatives of any quantity q . In the present implementation, the double stresses in the boundary are taken as zero:

$$P_i^t = 0 \quad (39)$$

$$\frac{Dq}{Dx_j} = \frac{\partial q}{\partial x_j} - \frac{\partial q}{\partial x_k} n_k n_j. \quad (40)$$

4.3 | Lagrange multipliers

The FEM simulation of second gradient media implies the use of C^1 discretisation functions for the displacement field as the second derivatives of the displacement are involved in the variational principle written in Equation 34. C^0 functions presents discontinuities in their first derivatives that would induce strong nonintegrable singularities of the second derivatives. A way to avoid the used of C^1 functions is to consider the second gradient medium as a particular case of a microstructured one.^{55,59} Therefore, a microstrain tensor v_{ij}^t and a microstress tensor λ_{ij}^t are introduced and the balance equation (Equation 34) now reads as follows:

$$\int_{\Omega^t} \left(\sigma_{ij}^t \frac{\partial u_i^*}{\partial x_j^t} + \Sigma_{ijk}^t \frac{\partial v_{ij}^*}{\partial x_k^t} \right) d\Omega^t - \int_{\Omega^t} \lambda_{ij}^t \left(\frac{\partial u_i^*}{\partial x_j^t} - v_{ij}^* \right) d\Omega^t - \bar{P}_e^* = 0, \quad (41)$$

where v_{ij}^* is virtual microstrain field. Consistently with that modified weak formulation of the balance equation, the external virtual power is rewritten as

$$\bar{P}_e^* = \int_{\Omega^t} \rho^t f_i^t u_i^* d\Omega^t + \int_{\Gamma_\sigma^t} (p_i^t u_i^* + P_i^t v_{ik}^* n_k^t) d\Gamma^t. \quad (42)$$

It can be seen that Equation 41 only displays first-order derivatives which permits to use of C^0 discretisation functions.

In order that the second gradient medium could be dealt with as a microstructure one, it is necessary to enforce the constraint $v_{ij}^t = \partial u_i^t / \partial x_j$ linking the microstrain and the displacement gradient. Still, to avoid the use of C^1 functions, this constraint is satisfied in a weak form that reads as follows :

$$\int_{\Omega^t} \lambda_{ij}^* \left(\frac{\partial u_i^t}{\partial x_j^t} - v_{ij}^t \right) d\Omega^t = 0. \quad (43)$$

The field λ_{ij}^* is the virtual counterpart of the microstress tensor. That weak formulation is equivalent to the strong one $v_{ij}^t = \partial u_i^t / \partial x_j$ and can lead to a locking of a FEM simulation; it has to be weakened by a suitable choice of the discretisation of the virtual microstress.

4.4 | Constitutive equations—second-order coefficients

A second gradient modelling needs constitutive equations for both the stress σ and the double stress Σ . As for the microstress λ , it is a Lagrange's multiplier and, as the pressure in a incompressible material, it cannot be the subject of a constitutive equation.

In the use of the second gradient modelling as a regularisation technique of a possibly singular first gradient problem, the first gradient constitutive equation is often that of the initial medium,⁵⁷ in the present paper this constitutive equation, concerning σ , is provided by the microscale homogenisation. Because of the lack of actual characteristics of second gradient material, the corresponding constitutive equation, concerning Σ , is taken as simple as possible, that is to say in a form suitable to large deformations, nonetheless satisfying the frame invariance principle and involving only one independent parameter D , see van den Eijnden et al⁶⁰:

$$\begin{bmatrix} \nabla \\ \Sigma_{111} \\ \nabla \\ \Sigma_{112} \\ \nabla \\ \Sigma_{121} \\ \nabla \\ \Sigma_{122} \\ \nabla \\ \Sigma_{211} \\ \nabla \\ \Sigma_{212} \\ \nabla \\ \Sigma_{221} \\ \nabla \\ \Sigma_{222} \end{bmatrix} = \begin{bmatrix} D & 0 & 0 & 0 & 0 & D/2 & D/2 & 0 \\ 0 & D/2 & D/2 & 0 & -D/2 & 0 & 0 & D/2 \\ 0 & D/2 & D/2 & 0 & -D/2 & 0 & 0 & D/2 \\ 0 & 0 & 0 & D & 0 & -D/2 & -D/2 & 0 \\ 0 & -D/2 & -D/2 & 0 & D & 0 & 0 & 0 \\ D/2 & 0 & 0 & -D/2 & 0 & D/2 & D/2 & 0 \\ D/2 & 0 & 0 & -D/2 & 0 & D/2 & D/2 & 0 \\ 0 & D/2 & D/2 & 0 & 0 & 0 & 0 & D \end{bmatrix} \begin{bmatrix} \frac{\partial \dot{v}_{11}}{\partial x_1} \\ \frac{\partial \dot{v}_{11}}{\partial x_2} \\ \frac{\partial \dot{v}_{12}}{\partial x_1} \\ \frac{\partial \dot{v}_{12}}{\partial x_2} \\ \frac{\partial \dot{v}_{21}}{\partial x_1} \\ \frac{\partial \dot{v}_{21}}{\partial x_2} \\ \frac{\partial \dot{v}_{22}}{\partial x_1} \\ \frac{\partial \dot{v}_{22}}{\partial x_2} \end{bmatrix}, \quad (44)$$

where \dot{v}_{ij} is the material derivative of v_{ij} , and Σ_{ijk} is the Jaumann double stress derivative defined by

$$\nabla_{ijk} = \dot{\Sigma}_{ijk} + \Sigma_{ijk}\omega_{li} + \Sigma_{imk}\omega_{mj} + \Sigma_{ijp}\omega_{pk} \quad (45)$$

in which ω_{li} is the spin tensor.

The internal length is not explicitly given in the formulation, it depends on the relation between the first and second-order coefficients, which is a priori unknown. A series of parametric simulations can serve to set this relationship.

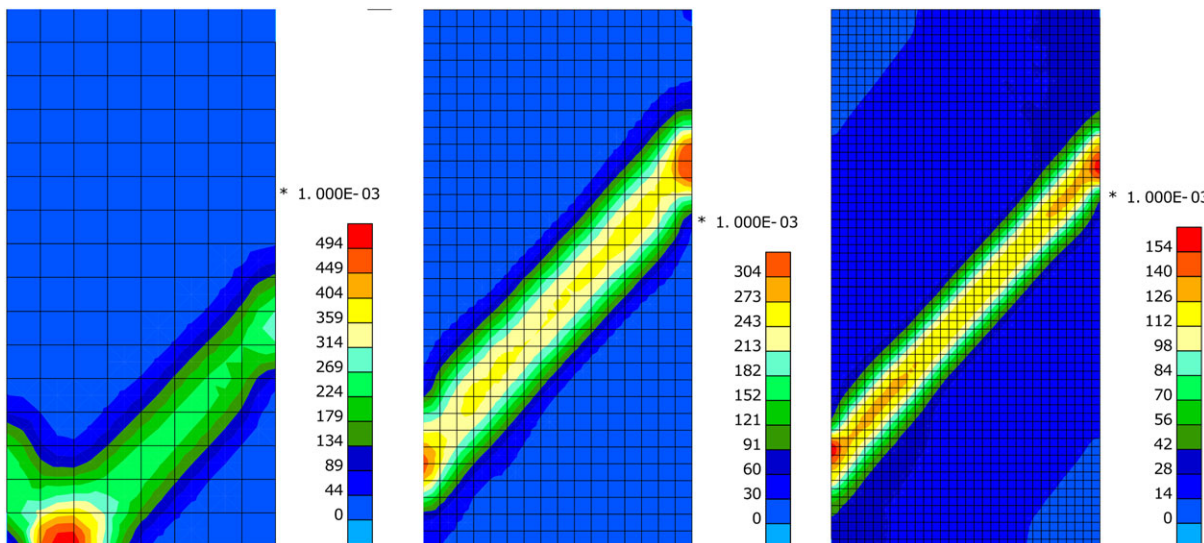


FIGURE 12 Biaxial compression test boundary value problem with different mesh sizes. The represented scalar is the total deviatoric strain [Colour figure can be viewed at wileyonlinelibrary.com]

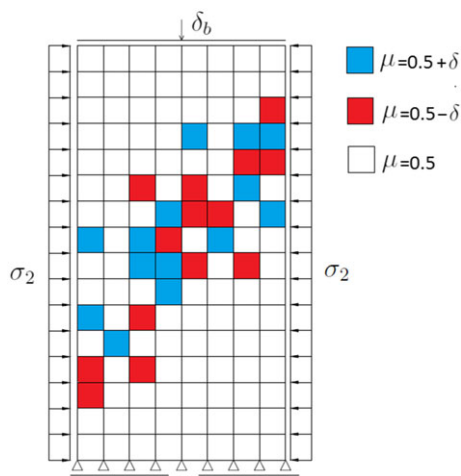


FIGURE 13 Biaxial test geometry and material point distribution over the elements $\delta=0.2/0.1/0.05/0.025$ ²⁸ [Colour figure can be viewed at wileyonlinelibrary.com]

4.5 | Second gradient efficiency assessment on biaxial compression test

The effect of the second gradient is illustrated in Figure 12. A standard compression biaxial test is modelled using three different mesh refinements (128, 512, and 2048 elements).

This regularisation not only enriches the physics of the model but also accelerates the simulation due to an improvement of the iterative efficiency, ie, a regularised problem has less possible solutions. The fact that the test with 128 elements exhibits a different localisation mode than the two other tests may be due to a characteristic length introduced by the second gradient terms not large enough with respect to the mesh characteristic size; in other words, a more refined mesh is required to obtain a reliable FE solution. Nevertheless, the reader should keep in mind that the provided solution for each test is only one of the multiple possible solutions, since the initial boundary value problem is perfectly homogeneous. Any shear band location is a correct solution to the problem, but the thickness and the orientation of the band are preserved when changing the mesh: Second gradient does heal the well-known spurious mesh dependency effect.

5 | SPATIAL VARIABILITY

The initial homogeneity, resulting from methodological reductionism of numerical models, can lead to radically different results compared with the ones of reality. In Fauchille et al,⁶¹ the symmetry breaking concept is used to show some of the drawbacks of reductionism.

5.1 | Symmetries and numerical models

The symmetries in a physical system are the states of this system that are equally seen from different perspectives. The existence of symmetries in a mechanical problem can lead to symmetrical solutions, which are very unlikely to happen in reality. In addition, the symmetric solution does not usually represent the minimum energy state of the system, so the numerical solution tends to overestimate the structure strength. Another effect of the existence of symmetries is the reduced performance of iterative methods such Newton when approaching a symmetry breaking because of the existence of different solutions. A solution to both numerical and physical issues derived from initial homogeneity is the introduction of heterogeneity in the form of spatial variability. An example of variability used in classical FEM models can be found in Chambon et al⁶² where modes of improbable slope failures are evaluated. Variability can also be introduced in the microscale in multiscale approaches, eg, FEM².⁶³

5.2 | Application to FEM×DEM

The FEM×DEM double-scale approach allows to introduce material heterogeneity from the microscale in different manners, eg, generating random realisations of the grain positions when generating the grain assembly.³² In the following case,

the particle friction angle is retained to introduce material variability. A series of simulations is prepared: a 128-element FEM biaxial sample is filled with 28 heterogeneous elements: Half of them with a decreased contact friction in the DEM assembly and the other half with increased contact friction leading to a nonbiased average of the friction angle with respect the reference value $\mu = 0.5$. As illustrated in Figure 13, this nonbiased set of elements is “randomly” distributed along a diagonal orientation in order to break the sample spatial homogeneity and determine the shear band orientation.

5.3 | Results

A parametric study is carried out with the values $\delta = 0.2/0.1/0.05/0.025$ being δ the variability of the contact friction coefficient. The second invariant of strain (Figure 14) shows a more regular and straight shear band for the lower values of δ (nearer to homogeneous state), with maximum values of shear strain similar for all cases, from less to more homogeneous: 24.3%, 22.3%, 21.7%, and 25.2%.

The elements with less contact friction in the DEM assemblies present sliding contacts earlier while the elements with higher contact friction are able to withstand more shear without sliding. This autocatalytic process triggers strain localisation earlier than in the case with an initially homogeneous state. The early elasto-plastic region I^{40} and the residual shear stress for large strain are similar or identical in all simulations while the peak stress values are slightly lower for the cases with higher δ : The main effect of the material variability is during the localisation process. It is worth remarking that even the case with smallest δ has a typical heterogeneous material behaviour differently from the initially homogeneous cases

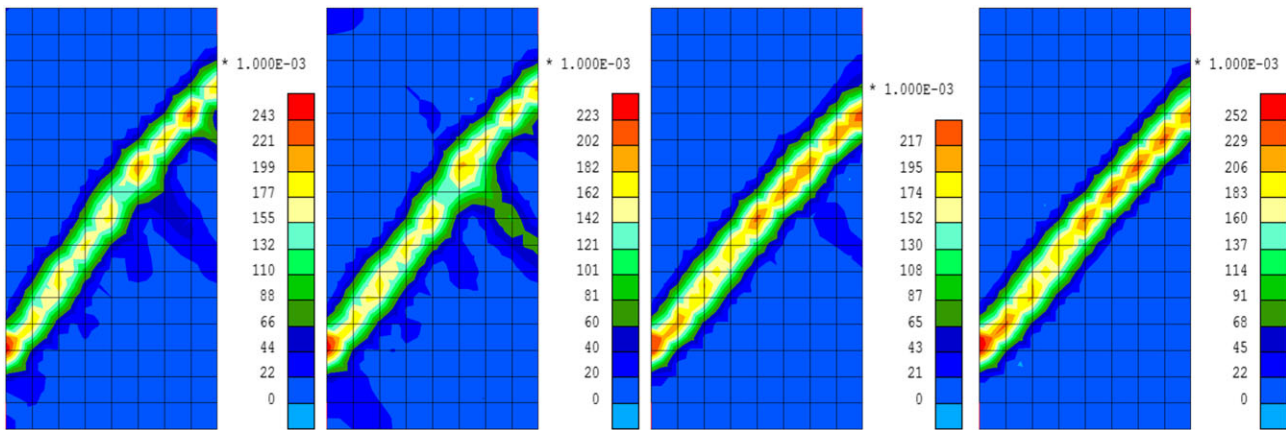


FIGURE 14 Second invariant of total strain at the end of a biaxial compression test ($\epsilon = 2.5\%$) for the parametric study of material point variability. From left to right: $\delta = 0.2, 0.1, 0.05, 0.025^{28}$ [Colour figure can be viewed at wileyonlinelibrary.com]

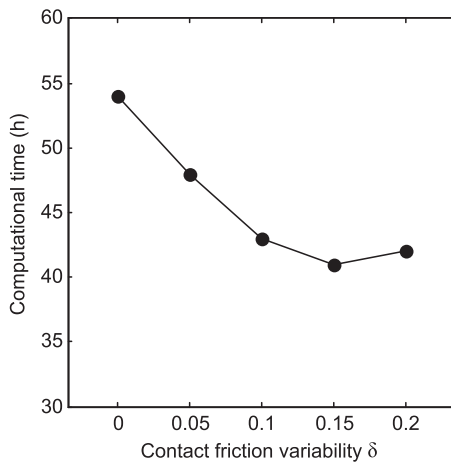


FIGURE 15 Computational time for parametric study of material point variability. The x axis shows the introduced variability parameter δ , zero meaning an homogeneous configuration

with $\delta = 0$: A small finite heterogeneity is able to trigger strain localisation earlier than the heterogeneity introduced by the numerical rounding, which is the only responsible of the break of symmetry in initially homogeneous material cases.

As localisation is accelerated, the Newton method becomes more efficient, converging to a solution in less iterations. Quantitative data of computational time are obtained using an Intel core i7 2620M processor. Results are presented together with the previous homogeneous case ($\delta = 0$) (Figure 15) showing a decrease of the computational time as the sample increases the heterogeneity: from 54 hours for the homogeneous case to 41 hours for $\delta = 0.15$, ie, a reduction of 24% of computational time.

6 | REAL-SCALE BOUNDARY VALUE PROBLEMS

In order to illustrate the capability of the model, real-scale problems are presented: laboratory scale problem (Biaxial test) and engineering scale problem (gallery excavation, pressuremetre test).

6.1 | Biaxial tests

Here, we present the results of a 2D FEM (plane strain) 3D DEM simulation using second gradient. The efficiency of the second gradient technique in restoring mesh independency has been illustrated in Section 4.5, using a 2D DEM model.

As shown in previous work of the same authors²⁶ or in Germain,⁵⁷ it is well known that implementing strain softening constitutive laws in FEM produces mesh dependency: The deformation concentrates in zones as narrow as the mesh permits, independent of any material parameter. In order to restore a mesh independent behaviour in such computations, an enrichment of the constitutive model following^{57,64} is used. This enrichment, described in this paper in Section 4 involves the addition of a second gradient term to the constitutive model, the classical (first gradient) part being still given by the NHL DEM described above.

Figure 16A presents the geometry and boundary conditions of biaxial test simulations. The constant confining pressures σ_2 is applied on the lateral sides and a vertical displacement at constant velocity is imposed on the top surface of the sample.

The domain is discretized by using 128 (first case) or 512 (second case) 2D FEM elements implementing second gradient (see Figure 16B). These elements use eight nodes for the macro kinematic field (displacement field u_i), four nodes for the micro-kinematic field (micro deformation gradient v_{ij}) and one node for a Lagrange multiplier λ_{ij} which is used to impose the equality of the microscopic and the macroscopic deformation gradient. Details about the second gradient method can be found in Germain⁵⁷ or Arcamone and Tritsch.⁶⁴

At the microscale level, identical EVs of 1000 spheres are used at each Gauss point. The volume is isotropically loaded, and all contacts are compressive but with adhesion: This represents a frictional granular material with cohesive bonds, eg, a unsaturated sand with capillary bridges in-between the sand grains. The microscopic parameters have been chosen according to classical dimensional analysis: (1) the stiffness ratio is $k_n/k_t = 1$, (2) the cohesion force f_c is defined so that $p^* = 1$, (3) the normal stiffness k_n is defined to obtain a stiffness parameter $\kappa = k_n/\sigma_0 = 500$, and (4) the intergranular coefficient of friction is $\mu = 0.5$.

Figure 17 that uses the second invariant of strain tensor shows the shear band at $\varepsilon_{11} = 10\%$, for two different mesh sizes. When using a first gradient model, shear bands tend to concentrate into a band of one element width.²⁶ In the present case, as result of second gradient model effect, shear band consists now of few elements. From this figure, it can be checked that the observed width of the shear band is intrinsic and independent of the mesh size.

6.2 | Gallery excavation and pressuremetre tests

The BVP for both gallery excavation and pressuremetre test consists in a hollow cylinder (Figure 18).⁶⁶ Being in the case of a gallery excavation or a pressuremetre test will depend on the loading path: decrease or increase of internal pressure respectively. The loading is force controlled both in the inner and outer boundaries.

A radial structured mesh is used in the FEM discretisation, using the same elements as shown in Figure 16B : 8+1 nodes elements with 4 Gauss points; the ninth node is placed in the centre of the element and is used by the second gradient implementation. To make the problem complete, 3 DOFs are restricted in order to avoid kinematic indetermination.

$$l_{SG} = \alpha \sqrt{D} \quad (46)$$

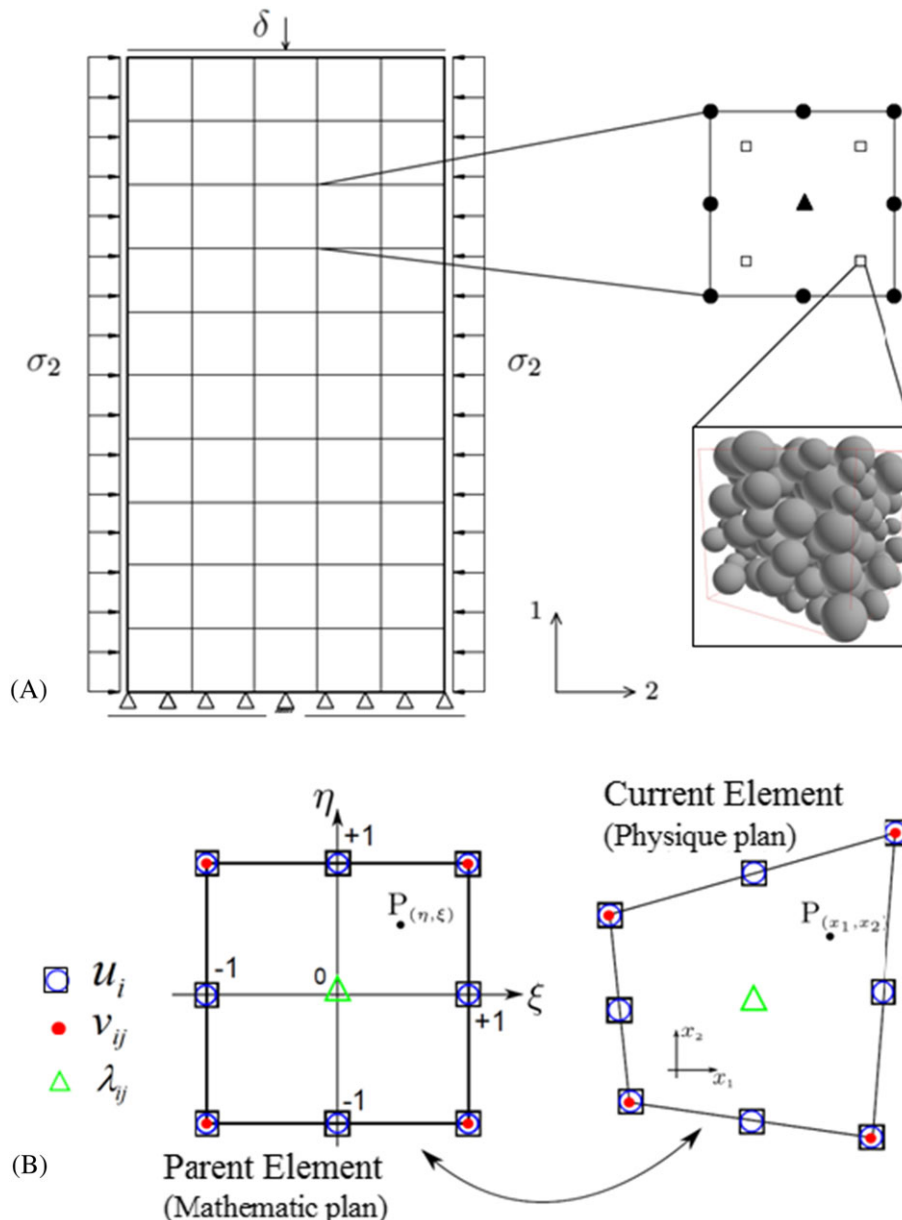


FIGURE 16 A, Spatial discretisation of the problem; B, element enriched for the second gradient technique⁶⁵ [Colour figure can be viewed at wileyonlinelibrary.com]

Being α a variable depending on the first gradient modulus, l_{SG} the characteristic length and D the second gradient parameter.

6.2.1 | Gallery excavation

A loading path consisting in a decrease of the internal pressure is applied. It emulates the deconfining occurring around the gallery during its excavation. For the present configuration, strain localisation in shear band mode does not manifest even when the internal pressure becomes zero. In order to reach the onset of strain localisation, the outer pressure has been increased once the inner pressure is zero. Two cases are considered, one with an initially isotropic far field stress state and another with an initially anisotropic far field stress state (Table 4). The results present strains around the excavation wall without clear definition of shear bands (Figure 19).

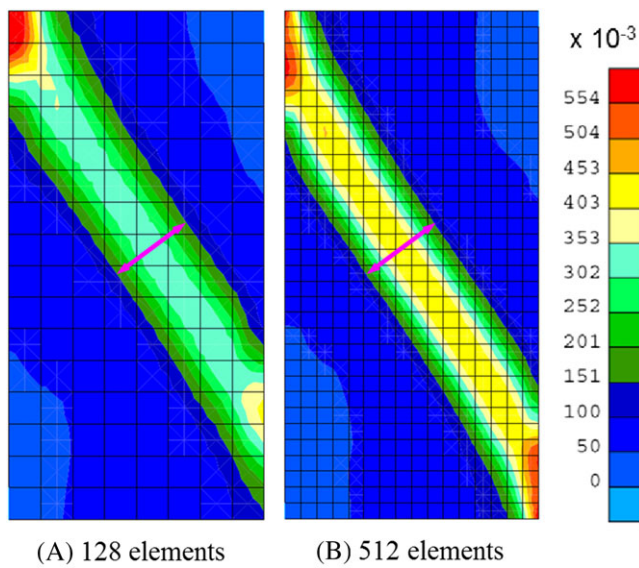


FIGURE 17 Map of the second invariant of the total strain tensor at $\epsilon_{11} = 10\%$ for (A) 128 elements and (B) 512 elements. The pink arrows superposed to the map are set with exactly the same length [Colour figure can be viewed at wileyonlinelibrary.com]

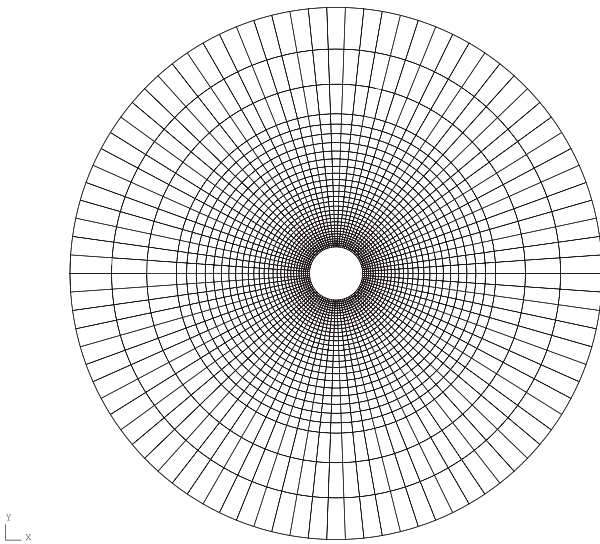


FIGURE 18 Standard hollow cylinder geometry used, inner radius = 10 m, outer radius = 100 m, 2700 Q8 elements, 160 boundary elements²⁸

TABLE 4 Loading path study: output data

Loading Path (Internal Pressure)	σ_{V0}/σ_{H0}	Force Multiplier	Max. VM Strain, %
Decrease	Isotropic 1/1	3.12	15.5
Decrease	Anisotropic 1.3/1	2.56	12.7

The two simulations end because of loss of controllability of the loading path. The following table summarises the initial stress states, force multiplier at the end of controllability, and maximum strains (Table 4). The initially anisotropic state reaches the end of controllability earlier than the initially isotropic case.

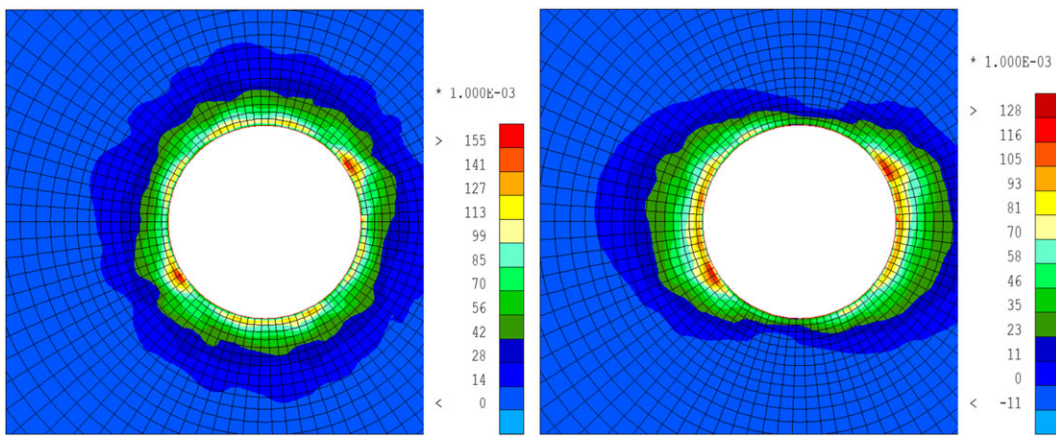


FIGURE 19 Results for the decrease of inner pressure. Two initial states: isotropic and anisotropic far field stress state. Second invariant of total strain at the end of the test. [Colour figure can be viewed at wileyonlinelibrary.com]

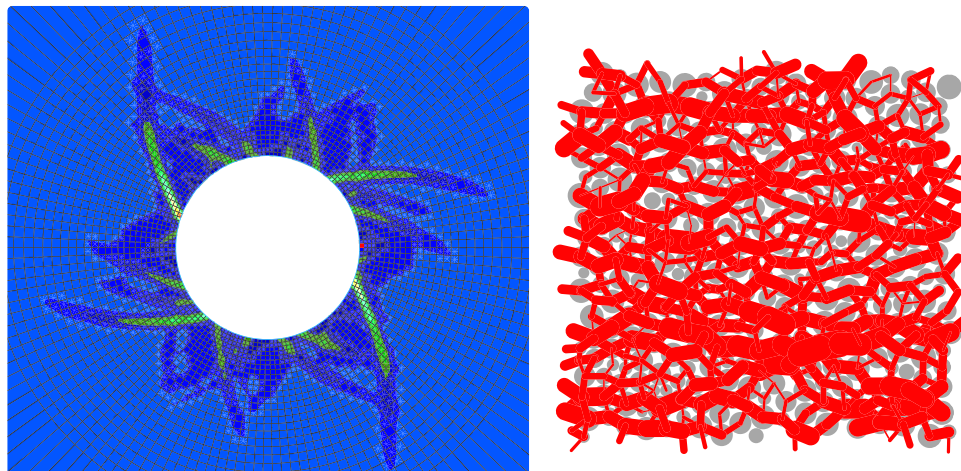


FIGURE 20 Left: Results for an isotropic hollow cylinder test, increase of internal pressure, final inner pressure = 4.15. The red element contains the DEM assembly shown in the right. Right: DEM assembly at the end of the loading, the red lines represent the contact forces. The orientation of the force chains is in accordance with the macroscale boundary condition²⁸ [Colour figure can be viewed at wileyonlinelibrary.com]

6.2.2 | Pressuremetre

The first pressuremetre BVP consists in a hollow cylinder, internal radius 10 m, external radius 100-m FEM mesh consisting of 4950 elements, 18 900 nodes, and 66 297 DOF (Figure 20). The initial confining pressure $p_0 = 1$, loading history, consists in an increase of the inner pressure, which in the initial condition is in equilibrium with the confining pressure $p_{in} = 1$.

The results show the formation of shear bands around the gallery (Figure 20). A DEM assembly at the end of the loading is also presented (Figure 20); this DEM assembly is located in the middle-right point in the inner part of the cylinder, indicated in red in (Figure 20).

The loading path corresponding to the increase of inner pressure (pressuremetre) leads to a more localised result compared to the gallery excavation (Figures 19 and 20). Several sets of shear bands appear around the pressuremetre (Figure 20), while in the case of the gallery excavation, the plastification zone is more diffuse without clear definition of shear bands (Figure 19).

This is a force controlled test; the increase of inner pressure governs the shear band evolution till the loss of controllability of the loading path.⁶⁷ This shows that the model can be applied to engineering scale configurations, with any mesh refinement, without suffering from pathological mesh dependency thanks to the second gradient regularisation.

Second gradient efficiency assessment on the pressuremetre test

As in the upper paragraph, a pressuremetre test is considered: The confining pressure is kept constant and equal to the initial pressure while the pressure inside the cylinder is increased. Two parametric cases are used to validate the relation 46, which correlates second gradient parameter with the shear band width. In these two cases, the mesh is the same, but the second gradient parameter D is different : $5 \cdot 10^{-2}$ and $5 \cdot 10^{-1}$, resulting in different shear band widths as can be seen in Figure 21. The asymmetry observed in the shear banding is generated by the initial deformation of the microscale (47); this initial deformation results from the relaxation step performed in order to equilibrate the out of balance shear stress of the microscale with the macroscopic boundary conditions.

$$\epsilon_{kl} = \begin{pmatrix} -0.9999 & 6.2850 \times 10^{-2} \\ 6.2850 \times 10^{-2} & -1.0000 \end{pmatrix} \quad (47)$$

The two simulations present slight differences in the localisation mode; this causes the second simulation to reach the end of controllability earlier and so experience more convergence difficulties (Table 5).

This example shows that second gradient enhancement of the constitutive law efficiently controls the shear band width not only in laboratory scale biaxial tests but also in real-scale engineering problems.

It is worth noting here that the results presented were obtained with a 2D DEM micro model, but the second gradient method, belonging entirely to the macroscale FEM model, can be used without any modification with 3D DEM micro models. Results with second gradient and 3D micro model are presented in the sequel.

FEM2D×DEM3D modelling of pressuremetre test

Although the NHL DEM model implemented in the case is a 3D model, it can be used in plane strain, plane stress, and 3D FEM models. Here, we discuss a comparison of several plane strain BVPs, using 2D finite elements.

The simulation presented predicts the response of the material in the midplace section of a pressuremetre, assuming plane strain condition in the axial direction.

In this simulation, only one-fourth of a plane section is modelled. This choice imposes arbitrarily vanishing values to the double stress tractions on the vertical and horizontal boundaries, which would not occur in a full domain simulation. However, this geometrically reduced model is used here for the sake of computing cost reduction, because the simulation only aims to demonstrate how the second gradient works in FEM2D×DEM3D framework and could regularise the problem. Full domain simulations like those illustrated in Figures 18 to 21 will be performed in next future. The domain is discretized using either first gradient element (Q8: 8 nodes, 4 Gauss points) or second gradient element (Q8+1, cf Figure 16B). The computation was performed as follows: Starting from a homogeneous state of isotropic compression,

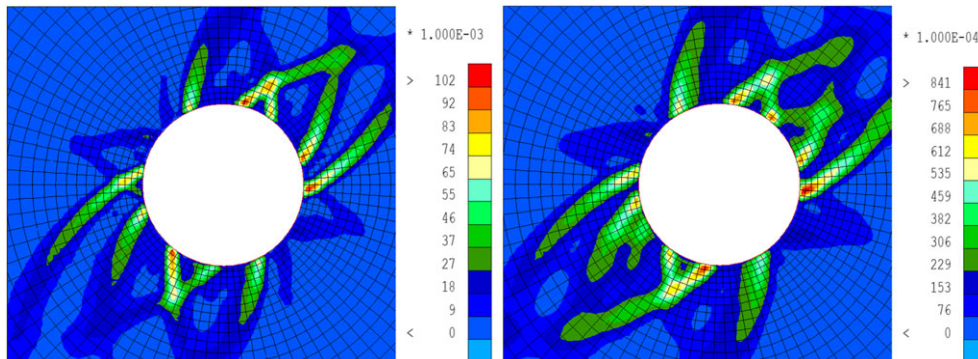


FIGURE 21 Pressuremetre test. The scalar represented is the second invariant of strain at the end of the test for the two configurations which differ by the values of the second gradient parameter: $5 \cdot 10^{-2}$ (left) and $5 \cdot 10^{-1}$ (right). The right figure shows the increase of shear band width determined by the second gradient parameter²⁸ [Colour figure can be viewed at wileyonlinelibrary.com]

TABLE 5 Second gradient study: output numerical

Second Gradient Parameter (D)	Number of Iterations	Number of Steps	Non-conv Steps	Wall-clock Time (d)	Max. VM Strain %
$5 \cdot 10^{-2}$	383	205	0	0.96	8.58
$5 \cdot 10^{-1}$	411	205	43	4.85	8.36

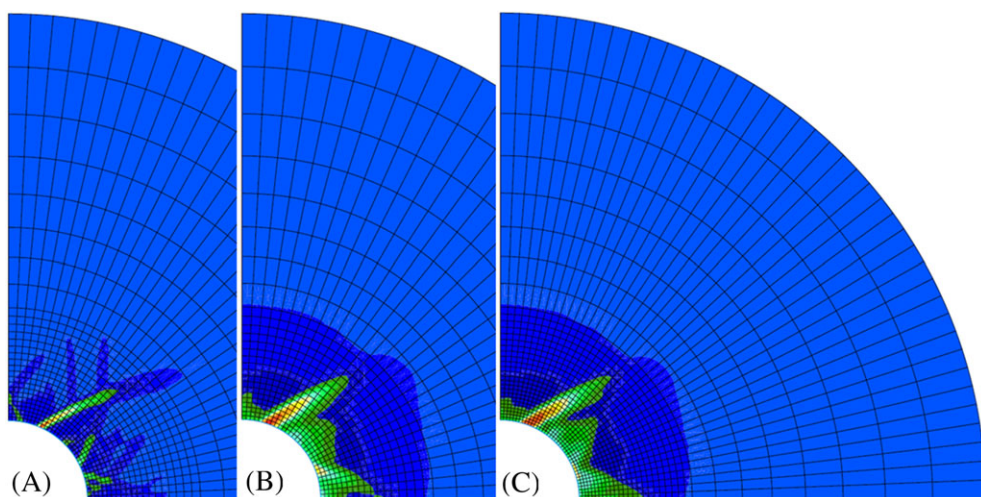


FIGURE 22 Multiscale modelling of the internal pressurisation of a hollow cylinder: (A) without second gradient regularisation; (B) second gradient regularisation, coarse mesh; (C) second gradient regularisation, finer mesh [Colour figure can be viewed at wileyonlinelibrary.com]

the internal pressure (σ_{int}) was increased up to 4 times of the initial isotropic stress, while the external pressure (σ_{ext}) was kept constant.

Figure 22 shows the deformation mode in the model at the end of the loading, in terms of the second invariant of strain tensor: (A) mesh with 952 standard Q8 elements (first gradient, ie, no regularisation) and (B,C) enriched elements (second gradient), two different meshes using 870 (B) or 1280 (C) elements. In the three cases presented in this figure, strain localisation has taken place, organised in shear bands originated at the internal wall and progressing significantly inside the cylinder. This is the result of the inherent strain softening exhibited by the materials. In panels B and C, the thickness of the shear bands does not depend on the mesh size, while in panel A, not using second gradient regularisation, it concentrates into a single layer of elements. These results demonstrate the capacity of the multiscale approach to account for complex failure patterns. It is shown again that the second gradient method mitigates efficiently the mesh dependency problem observed with classical (first gradient) constitutive models.

7 | CONCLUDING REMARKS

In this paper, we have introduced a double-scale integrated numerical approach of boundary value problems involving granular materials. Two different numerical modelling methods are used, namely, FEM at the macroscale and DEM at the microscale. A large discussion of the computing scheme involved has been presented, developing in details how DEM applied to a volume element figuring a limited in size granular assembly can be used to generate, step by step along the overall computation process, a consistent constitutive law that we call NHL for *Numerically Homogenised Law*. It is shown that attaching such an elementary volume to every Gauss point in a FEM model and submitting it to the local deformation gradient allows to define the stress state and a pseudotangent operator for the Gauss point considered. As in any classical FEM process, these local data are assembled into the global stiffness matrix and the global force vector, which defines the linear system to be solved for the current iteration of the Newton-Raphson loop, leading eventually to a converged solution of the current step of the macroscale boundary problem. Parallelisation is almost mandatory when implementing double-scale integrated numerical methods, because of the CPU-time challenge induced by the DEM microscale problems to be solved at each integration point of the FEM macroscale mesh. Several strategies have been used; they are described and commented in Section 3. Using FEM at the macroscale enables one to take advantage of the well-established continuum framework including advanced tools such as multiscale coupling (not developed in the present paper) or higher order constitutive frameworks used to mitigate the well-known mesh-dependency spurious effect in case of strain localisation: The latter has been developed in Section 4 and illustrated in Section 6 devoted to examples of real-scale BVPs.

We addressed as well the interesting question of spatial variability, which can be introduced at no extra computing cost in the present framework, either on a statistical point of view to take into account the inherent variability of a real granular mass, as homogeneous as it can be seen at the macroscopic scale, or to model a spatially organised variability of the material, eg, layers observed in situ in a granular deposit.

In conclusion, we would like to discuss two possible understandings of the approach. In the first point of view, the FEM could be seen as an overlayer to the DEM that makes possible the simulation of systems like huge engineered structures, while continuing to benefit from the particle-based strategy. We stress that the original conception is actually different—but not contradictory—in the authors' mind: The DEM is thought as a way to obtain a *master law* able to face any complexity in the loading path that may involve strain (multi)localisation, specific path, pressure dependence, or whatever. With this second point of view, the resulting model is potentially far richer than any constitutive model expressed with mathematical relations.

Obviously, the benefits of the approach do not come without a cost. The first cost to think of is of course the computing time. This can, and in fact this must, be mitigated using parallel computing, as massive as possible. Parallel computing for FEMxDEM is extremely efficient, because most of the computing time is spent in the microscale BVPs, allowing for a massive reduction of the computing time as the number of threads used increases. The OpenMP parallelisation framework is a shared memory model; it is rather easy to implement in an existing FEM code but the number of threads is limited by the necessity that all the threads have to access to the same memory. Conversely, an MPMD framework with distributed memory can be used. It relaxes the above constraint and allows to increase the number of threads used in the concurrent computing process.

Another cost induced by the use of a DEM-based NHL is the difficulty in deriving a consistent tangent operator directly, or even by numerical derivation due to the severe fluctuations of the response of the micro model as soon as it enters in a strain-softening loading range. Solutions for this problem have been presented in Section 2.5.2.

A point that can be risen is what seems to be a lack of link between the microscale and the macroscale with regard to the internal length introduced in the second gradient model. It may be considered that the internal length should derive from the microscale computation. However, observations of localised phenomena in geomechanics and geophysics seem to indicate that strain localisation is a multiscale process, whose observed characteristics depend on the scale of observation. For example, digital image correlation of satellite radar-data of the Arctic sea ice cover over a 3-day time period shows that deformation of this very large solid body for scales from 10 to 1000 km is localised at different scales and can be characterised as multifractal.⁶⁸ Also, recent experimental results⁶⁹ obtained using 3D digital image correlation on high-resolution X-ray tomography images of standard geotechnical size (70 mm) sand specimens subjected to triaxial tests show early localised deformation events proliferating inside the specimens at a smaller scale than the shear bands that will be observed later on in the test. So the adopted approach consisting in specifying an internal length directly at the macroscale, based on in situ observations at the relevant scale, is not less reasonable than extracting it from the microscale model: Actually, the latter is supposed only to provide a realistic stress-strain response for a granular media.

Altogether, double-scale FEM-DEM approach is a most promising way to take into account the specificities of granular media in modelling real-scale problems, with characteristic size of the studied domain several order of magnitude larger than the characteristic size of microstructure.

ACKNOWLEDGEMENT

This work was carried out in the framework of projects ANR-MicroModEx and ANR-GeoBridge at 3SR Lab. The authors would like to thank ANR (French National Research Agency) for this support. The laboratory 3SR is part of the LabEx Tec 21 (Investissements d'Avenir—grant agreement No. ANR-11-LABX-0030). Most of the computations presented in this paper were performed using the GRICAD infrastructure (<https://gricad.univ-grenoble-alpes.fr>), which is partly supported by the Equip@Meso project (reference ANR-10-EQPX-29-01) of the programme Investissements d'Avenir supervised by the Agence Nationale pour la Recherche.

ORCID

Jacques Desrues  <https://orcid.org/0000-0002-5514-2458>
 Stefano Dal Pont  <https://orcid.org/0000-0002-0348-5918>

REFERENCES

1. Cundall PA, Strack ODL. A discrete numerical model for granular assemblies. *Géotechnique*. 1979;29(1):47-65.
2. Guo N, Zhao J. A hierarchical model for cross-scale simulation of granular media. *AIP Conf Proc*. 2013;1542(1):1222-1225.
3. Kanouté P, Boso DP, Chaboche JL, Schrefler BA. Multiscale methods for composites: a review. *Arch Comput Meth Eng*. 2009;16(1):31-75.
4. Geers MGD, Kouznetsova VG, Brekelmans WAM. Multi-scale computational homogenization: trends and challenges. *J Comput Appl Math*. 2010;234(7):2175-2182. Fourth International Conference on Advanced COmputational Methods in ENgineering (ACOMEN 2008).

5. van den Eijnden AP, Bésuelle P, Chambon R, Collin F. A FE2 modelling approach to hydromechanical coupling in cracking-induced localization problems. *Int J Solids Struct.* 2016;97-98:475-488.
6. van den Eijnden AP, Bésuelle P, Collin F, Chambon R, Desrues J. Modeling the strain localization around an underground gallery with a hydro-mechanical double scale model: effect of anisotropy. *Comput Geotech.* 2017;85:384-400.
7. Gudehus G. A comparison of some constitutive laws for soils under radially symmetric loading and unloading. In: Proc. 3rd Int. Conf. Num. Meth. Geomech. Balkema; 1979; Aachen:1309-1324.
8. Tamagnini C, Calvetti F, Viggiani G. An assessment of plasticity theories for modeling the incrementally nonlinear behavior of granular soils. *J Eng Math.* 2005;52(1):265-291.
9. Borja RI, Wren JR. Micromechanics of granular media part i: generation of overall constitutive equation for assemblies of circular disks. *Comput Meth Appl Mech Eng.* 1995;127(1):13-36.
10. Wren JR, Borja RI. Micromechanics of granular media part ii: overall tangential moduli and localization model for periodic assemblies of circular disks. *Comput Meth Appl Mech Eng.* 1997;141(3):221-246.
11. Meier HA, Steinmann P, Kuhl E. Towards completeness, a multiscale approach of confined particulate systems. In: Visualization of Large and Unstructured Data Sets: Second Workshop of the DFG's International Research Training Group "Visualization Of Large And Unstructured Data Sets - Applications In Geospatial Planning, Modeling, And Engineering"; 2007; Kaiserslautern, Germany:103-114.
12. Rudnicki JW, Rice JR. Conditions for the localization of deformation in pressure-sensitive dilatant materials. *J Mech Phys Solids.* 1975;23(6):371-394.
13. Nitka M, Bilbie B, Combe G, Dascalu C, Desrues J. A micro-macro (DEM-FEM) model of the behavior of granular solids. In: 1st International Symposium On Computational Geomechanics (COMGEO I); 2009; Juan-les-Pins, France:38-48.
14. Andrade JE, Avila CF, Hall SA, Lenoir N, Viggiani G. Multiscale modeling and characterization of granular matter: from grain kinematics to continuum mechanics. *J Mech Phys Solids.* 2011;59(2):237-250.
15. Kaneko K, Terada K, Kyoya T, Kishino Y. Global-local analysis of granular media in quasi-static equilibrium. *Int J Solids Struct.* 2003;40(15):4043-4069.
16. Meier HA, Steinmann P, Kuhl E. Towards multiscale computation of confined granular media., *Technische Mechanik.* 2008;28(1):32-42.
17. Miehe C, Dettmar J. A framework for micro-macro transitions in periodic particle aggregates of granular materials. *Comput Meth Appl Mech Eng.* 2004;193(3-5):225-256.
18. Miehe C, Dettmar J, Zah D. Homogenization and two-scale simulations of granular materials for different microstructural constraints. *Int J Numer Methods Eng.* 2010;83(8-9):1206-1236.
19. Nitka M, Combe G, Dascalu C, Desrues J. Two-scale modeling of granular materials: a DEM-FEM approach. *Granular Matter.* 2011;13(3):277-281.
20. Guo N, Zhao J. A coupled FEM/DEM approach for hierarchical multiscale modelling of granular media. *Int J Numer Methods Eng.* 2014;99(11):789-818.
21. Guo N, Zhao J. 3d multiscale modeling of strain localization in granular media. *Comput Geotech.* 2016;80:360-372.
22. Guo N, Zhao J. Parallel hierarchical multiscale modelling of hydro-mechanical problems for saturated granular soils. *Comput Meth Appl Mech Eng.* 2016;305:37-61.
23. Ning G, Jidong Z. Multiscale insights into classical geomechanics problems. *Int J Numer Anal Methods Geomech.* 2015;40(3):367-390.
24. Wu H, Guo N, Zhao J. Multiscale modeling and analysis of compaction bands in high-porosity sandstones. *Acta Geotech.* 2018;13(3):575-599.
25. Nguyen TK, Combe G, Caillerie D, Desrues J. Modeling of a cohesive granular materials by a multi-scale approach. *AIP Conf Proc.* 2013;1542(1):1194-1197.
26. Nguyen T, Combe G, Caillerie D, Desrues J. FEM×DEM modelling of cohesive granular materials: numerical homogenisation and multi-scale simulations. *Acta Geophys.* 2014;62(5):1109-1126.
27. Desrues J, Nguyen TK, Combe G, Caillerie D. FEM×DEM multi-scale analysis of boundary value problems involving strain localization. In: Chau K-T, Zhao J, eds. *Bifurcation and Degradation of Geomaterials in the New Millennium*, Springer Series in Geomechanics and Geoengineering: Springer International Publishing; 2015:259-265.
28. Argilaga A. Femxdem double scale approach with second gradient regularization applied to granular materials modeling. *Ph.D. Thesis:* Communauté Université Grenoble Alpes; 2016.
29. Desrues J, Argilaga A, Dal Pont S, Combe G, Caillerie D, Kien Nguyen T. Restoring mesh independency in fem-dem multi-scale modelling of strain localization using second gradient regularization. In: Papamichos E, Papanastasiou P, Pasternak E, Dyskin A, eds. *Bifurcation and Degradation of Geomaterials with Engineering Applications*. Cham: Springer International Publishing; 2017:453-457.
30. Nguyen TK, Argilaga Claramunt A, Caillerie D, et al. FEM DEM: a new efficient multi-scale approach for geotechnical problems with strain localization. *EPJ Web Conf.* 2017;140:11007.
31. Argilaga A, Desrues J, Dal Pont S, Combe G, Caillerie D. FEM-DEM multiscale modeling: model performance enhancement from newton strategy to element loop parallelization. *Int J Numer Methods Eng.* 2018;114(1):47-65.
32. Shahin G, Desrues J, Dal Pont S, Combe G, Argilaga A. A study of the influence of REV variability in double scale FEM× DEM analysis. *Int J Numer Methods Eng.* 2016;107(10):882-900.
33. Kuhn MR, Chang CS. Stability, bifurcation, and softening in discrete systems: a conceptual approach for granular materials. *Int J of Solids and Structures.* 2006;43:6026-6051.
34. Allen MP, Tildesley DJ. *Computer Simulation of Liquids*. New York, NY, USA: Clarendon Press; 1989.

35. Radjai F, Voivret C. Periodic boundary conditions. In: et F Dubois FR, ed. *Discrete-Element Modeling of Granular Materials*: Wiley-Iste; 2011:181-198.
36. Richefeu V, Combe G, Viggiani G. An experimental assessment of displacement fluctuations in a 2d granular material subjected to shear. *Géotechnique Lett.* 2012;2(3):113-118.
37. Combe G, Richefeu V, Stasiak M, Atman APF. Experimental validation of a nonextensive scaling law in confined granular media. *Phys Rev Lett.* 2015;115:238301.
38. Midi G. On dense granular flows. *Eur Phys J E.* 2004;14:341-365.
39. Combe G, Roux J-N. Discrete numerical simulation, quasistatic deformation and the origins of strain in granular materials. ArXiv e-prints 2009 Jan; 2009.
40. Roux J-N, Combe G. Quasistatic rheology and the origins of strain. *CR Phys.* 2002;3(2):131-140.
41. Kruyt NP, Rothenburg L. Statistical theories for the elastic moduli of two-dimensional assemblies of granular materials. *Int J Eng Sci.* 1998;36(10):1127-1142.
42. Simo JC, Taylor RL. Consistent tangent operators for rate-independent elastoplasticity. *Comput Meth Appl Mech Eng.* 1985;48(1):101-118.
43. Nguyen TK. Modélisation numérique à double échelle des matériaux granulaires cohésifs : Approche par éléments finis-éléments discrets. *Ph.D. Thesis:* Université Grenoble Alpes; 2013.
44. Schneebeli G. Une analogie mécanique pour les terres sans cohésion. *Comptes Rendus de l'académie des Sci.* 1956;243(1):126-126.
45. Joer H, Lanier J, Desrues J, Flavigny E. “ $1/\gamma_2\epsilon$ ”: a new shear apparatus to study the behavior of granular materials. *Geotech Test J.* 1992;15(2):129-137.
46. Desrues J, Duthilleul B. Mesure du champ de déformation d'un objet plan par la méthode stéréogrammétique de faux relief. *J de Mécanique Théorique et Appliquée.* 1984;3:79-103.
47. Kruyt NP, Rothenburg L. Kinematic and static assumptions for homogenization in micromechanics of granular materials. *Mech Mater.* 2004;36(12):1157-1173.
48. Charlier R. Approche unifiée de quelques problèmes non linéaires de mécanique des milieux continus par la méthode des éléments finis. *Thèse de doctorat.* Belgium: Liège University; 1987.
49. Collin F. Couplages thermo-hydro-mécaniques dans les sols et les roches tendres partiellement saturés. *Thèse de doctorat.* Belgium: Liège University; 2003.
50. OpenMP ARB, OpenMP Application Program Interface. Version 3.1; 2011.
51. Moto Mpong S, de Montleau P, Godinas A, Habraken A. A parallel computing model for the acceleration of a finite element software. In: Proceedings of the International Conference On Parallel And Distributed Processing Techniques And Applications. CSREA Press; 2002; Las Vegas (Nevada), USA:185-191.
52. de Montleau P, Cela JM, Mpong SM, Godinass A. A parallel computing model for the acceleration of a finite element software. In: International Symposium on High Performance Computing. Springer; 2002:449-456.
53. Germain P. La méthode des puissances virtuelles en mécanique des milieux continus. *J Mécanique.* 1973;12:236-274.
54. Chambon R, Caillerie D, El Hassan N. One-dimensional localisation studied with a second grade model. *Eur J Mech A Solids.* 1998;17(4):637-656.
55. Mindlin RD. Micro-structure in linear elasticity. *Arch Ration Mech Anal.* 1964;16(1):51-78.
56. Chambon R, Caillerie D, Matsushima T. Plastic continuum with microstructure, local second gradient theories for geomaterials: localization studies. *Int J Solids Struct.* 2001;38(46):8503-8527.
57. Matsushima T, Chambon R, Caillerie D. Large strain finite element analysis of a local second gradient model: application to localization. *Int J Numer Methods Eng.* 2002;54(4):499-521.
58. Mindlin RD. Second gradient of strain and surface-tension in linear elasticity. *Int J Solids Struct.* 1965;1(4):417-438.
59. Germain P. The method of virtual power in continuum mechanics. part 2: microstructure. *SIAM J Appl Math.* 1973;25(3):556-575.
60. Bésuelle P, Chambon R, Collin F. Switching deformation modes in post-localization solutions with a quasibrittle material. *J Mech Mater Struct.* 2006;1(7):1115-1134.
61. Anderson PW. More is different. *Science.* 1972;177(4047):393-396.
62. van den Eijnden AP, Hicks MA. Efficient subset simulation for evaluating the modes of improbable slope failure. *Comput Geotech.* 2017;88:267-280.
63. Fauchille AL, van den Eijnden AP, Ma L, et al. Variability in spatial distribution of mineral phases in the lower bowland shale, uk, from the mm- to micro-scale: quantitative characterization and modelling. *Mar Pet Geol.* 2018;92:109-127.
64. Chambon R, Caillerie D, El Hassan N. One dimensional localisation studied with a second grade model. *Eur J Mechanics, A/Solids.* 1998;17(4):637-656.
65. Marinelli F, Sieffert Y, Chambon R. Hydromechanical modeling of an initial boundary value problem: studies of non-uniqueness with a second gradient continuum. *Int J Solids Struct.* 2015;54:238-257.
66. Arcamone J, Tritsch JJ. The cerchar method of pressiometric testing. *Min Sci Technol.* 1985;2(3):229-233.
67. Buscarnera G, Dattola G, Di Prisco C. Controllability, uniqueness and existence of the incremental response: a mathematical criterion for elastoplastic constitutive laws. *Int J Solids Struct.* 2011;48(13):1867-1878.
68. Marsan D, Stern H, Lindsay R, Weiss J. Scale dependence and localization of the deformation of Arctic sea ice. *Phys Rev Lett.* 2004;93(17):178501(1-4).

69. Desrues J, Andò E, Bésuelle G, et al. Localisation precursors in geomaterials? In: Papamichos E, Papanastasiou P, Pasternak E, Dyskin A, eds. *Bifurcation and Degradation of Geomaterials with Engineering Applications*, Series in Geomechanics and Geoengineering: Springer; 2017:3-10.
70. Truesdell CA. *A First Course in Rational Continuum Mechanics*: Academic Press; 1991.
71. Gurtin ME. *An Introduction to Continuum Mechanics*, Mathematics in Science and Engineering, vol. 158: Academic Press; 1981.

How to cite this article: Desrues J, Argilaga A, Caillerie D, et al. From discrete to continuum modelling of boundary value problems in geomechanics: An integrated FEM-DEM approach. *Int J Numer Anal Methods Geomech.* 2019;1–37. <https://doi.org/10.1002/nag.2914>

APPENDIX A: CHANGE OF REFERENCE FRAMES AND FRAME INVARIANCE

A frame is a system that enables to define the positions of the material points with vectors. There is an infinity of frames and if \vec{x} and $\tilde{\vec{x}}$ are the positions of a material point in two different frames there exist a vector \vec{X} and an isometry \mathbf{R} such that $\tilde{\vec{x}} = \vec{X} + \mathbf{R} \cdot \vec{x}$ for any material points. The reason of that form of the relation of change of frames is that it preserves the distances between material points. \vec{X} and \mathbf{R} may depend on the time and the derivation with respect to time yields the relation of change of frames for the velocities of the material points that reads $\tilde{\vec{v}} = \vec{V} + \Omega \cdot \tilde{\vec{x}} + \mathbf{R} \cdot \vec{v}$ where $\Omega = \dot{\mathbf{R}} \circ \mathbf{R}^T$ is the instantaneous rotation operator and where $\vec{V} = \dot{\vec{X}} - \Omega \cdot \vec{X}$. The change of frames for the velocities may also be written $\tilde{\vec{v}} = \vec{V} + \tilde{\vec{\Omega}} \wedge \tilde{\vec{x}} + \mathbf{R} \cdot \vec{v}$ where $\tilde{\vec{\Omega}}$ is the vector associated with the skew symmetric application Ω . The change of frames for the rotation velocity vector of an indeformable solid reads $\tilde{\vec{\omega}} = \vec{\omega} + \det \mathbf{R} \mathbf{R} \cdot \vec{\omega}$. As \mathbf{R} is an isometry then $\det \mathbf{R} = \pm 1$, it has to be noticed that \mathbf{R} is not necessarily a rotation.

The values of physical quantities as masses, kinetic energy, velocities, forces, deformation gradients, stress tensors and so on ... are frame dependent. A scalar quantity is said objective if its values are the same whatever is the frame, on principle masses are objective but kinetic energy is not. A vector quantity is said objective if the change of frames for it reads $\tilde{\vec{S}} = \mathbf{R} \cdot \vec{S}$, the difference of positions of two material points is objective but the difference of velocities is not, on principle the forces are objective vectors. A tensor quantity is said objective if the change of frame for it reads $\tilde{\mathbf{T}} = \mathbf{R} \circ \mathbf{T} \circ \mathbf{R}^T$.

More details about changes of frames and objectivity can be found in some textbooks of mechanics as Truesdell⁷⁰ or Gurtin.⁷¹

A.1 | Objectivity of the relative velocity $\tilde{\vec{V}}^r$ (Equation 6) and of the derivative (Equation 9) of \vec{f}_T

Taking into account the relations of change of frames, the relative velocity (see Equation 6) in another frame reads

$$\tilde{\vec{V}}^r = \tilde{\vec{\Omega}} \wedge (\tilde{\vec{x}}^m - \tilde{\vec{x}}^n) + \mathbf{R} \cdot (\tilde{\vec{v}}^m - \tilde{\vec{v}}^n) + (\tilde{\vec{\Omega}} + \det \mathbf{R} \mathbf{R} \cdot \tilde{\vec{\omega}}^m) \wedge (\tilde{\vec{P}} - \tilde{\vec{r}}^m) - (\tilde{\vec{\Omega}} + \det \mathbf{R} \mathbf{R} \cdot \tilde{\vec{\omega}}^n) \wedge (\tilde{\vec{P}} - \tilde{\vec{r}}^n)$$

that is to say, assuming that the definition of the contact point $\tilde{\vec{P}}$ depends only on the positions and the radii of the grains making contact and therefore is objective

$$\tilde{\vec{V}}^r = \mathbf{R} \cdot (\tilde{\vec{v}}^m - \tilde{\vec{v}}^n) + (\det \mathbf{R} \mathbf{R} \cdot \tilde{\vec{\omega}}^m) \wedge (\mathbf{R} \cdot (\tilde{\vec{P}} - \tilde{\vec{r}}^m)) - (\det \mathbf{R} \mathbf{R} \cdot \tilde{\vec{\omega}}^n) \wedge (\mathbf{R} \cdot (\tilde{\vec{P}} - \tilde{\vec{r}}^n))$$

now, as \mathbf{R} is an isometry, for any vector \vec{a} and \vec{b} , $(\mathbf{R} \cdot \vec{a}) \wedge (\mathbf{R} \cdot \vec{b}) = \det \mathbf{R} \mathbf{R} \cdot (\vec{a} \wedge \vec{b})$ and, as $\det \mathbf{R} = \pm 1$ it comes

$$\tilde{\vec{V}}^r = \mathbf{R} \cdot (\tilde{\vec{v}}^m - \tilde{\vec{v}}^n + \tilde{\vec{\omega}}^m \wedge (\tilde{\vec{P}} - \tilde{\vec{r}}^m) - \tilde{\vec{\omega}}^n \wedge (\tilde{\vec{P}} - \tilde{\vec{r}}^n)),$$

which is the expression of the objectivity of the relative velocity.

The relation of change of frame for the derivative of an objective vector is not so different from the relation for the velocity of a material point. It reads $\tilde{\vec{a}} = \tilde{\vec{\Omega}} \wedge \tilde{\vec{a}} + \mathbf{R} \cdot \dot{\vec{a}}$ where $\tilde{\vec{a}} = \mathbf{R} \cdot \vec{a}$. Consequently, the derivative of Equation 9 of \vec{f}_T in a change of frame reads

$$\overset{\circ}{\vec{f}}_T = \dot{\tilde{\vec{f}}}_T + (\dot{\tilde{\vec{f}}}_T \cdot \tilde{\vec{n}}) \tilde{\vec{n}} - P_{\tilde{\vec{n}}} \cdot \frac{1}{2} (\tilde{\vec{\omega}}^n + \tilde{\vec{\omega}}^m) \wedge \tilde{\vec{f}}_T$$

that is to say, using the different relations of change of frames

$$\begin{aligned}\overset{\circ}{\vec{f}_T} &= \vec{\Omega} \wedge \vec{f}_T + \mathbf{R} \cdot \dot{\vec{f}}_T + \left(\vec{f}_T \cdot (\vec{\Omega} \wedge \vec{n}) \right) \vec{n} + \left((\mathbf{R} \cdot \vec{f}_T) \cdot (\mathbf{R} \cdot \dot{\vec{n}}) \right) (\mathbf{R} \cdot \vec{n}) \\ &\quad - P_{\Pi} \cdot (\vec{\Omega} \wedge \vec{f}_T) - \mathbf{R} \cdot P_{\Pi} \cdot \mathbf{R}^T \cdot \frac{1}{2} \left(\det \mathbf{R} \mathbf{R} \cdot (\vec{\omega}^n + \vec{\omega}^m) \right) \wedge (\mathbf{R} \cdot \vec{f}_T),\end{aligned}$$

which yields

$$\overset{\circ}{\vec{f}_T} = \left(\mathbf{I} - \vec{n} \otimes \vec{n} - P_{\Pi} \right) \cdot \left(\vec{\Omega} \wedge \vec{f}_T \right) + \mathbf{R} \cdot \left(\dot{\vec{f}}_T + (\vec{f}_T \cdot \dot{\vec{n}}) (\vec{n}) - P_{\Pi} \cdot \frac{1}{2} ((\vec{\omega}^n + \vec{\omega}^m)) \wedge \vec{f}_T \right),$$

where \mathbf{I} denotes the identity tensor. As $\mathbf{I} - \vec{n} \otimes \vec{n} = P_{\Pi}$ that yields

$$\overset{\circ}{\vec{f}_T} = \mathbf{R} \cdot \left(\dot{\vec{f}}_T + (\vec{f}_T \cdot \dot{\vec{n}}) (\vec{n}) - P_{\Pi} \cdot \frac{1}{2} ((\vec{\omega}^n + \vec{\omega}^m)) \wedge \vec{f}_T \right),$$

which proves that $\overset{\circ}{\vec{f}_T}$ is an objective derivative of \vec{f}_T .